

The Influence of Gravitational Microlensing on the Broad Emission Lines of Quasars

C. Abajas¹, E. Mediavilla¹, J. A. Muñoz¹, L. Č. Popović², and A. Oscoz¹

abajas@ll.iac.es, emg@ll.iac.es, jmunoz@ll.iac.es,
lpopovic@aob.aob.bg.ac.yu, aoscoz@ll.iac.es

ABSTRACT

We discuss the effects of microlensing on the broad emission lines (BELs) of QSOs in the light of recent determinations of the size of the broad line region (BLR) and its scaling with QSO luminosity. Microlensing by star-sized objects can produce significant amplifications in the BEL of some multiple-imaged QSOs, and could be very relevant for high-ionization lines. We have identified a group of ten gravitational lens systems ($\sim 30\%$ of the selected sample) in which microlensing could be observed. Using standard kinematic models for AGNs, we have studied the changes induced in the line profile by a microlens located at different positions with respect to the center of the BLR. We found that microlensing could produce important effects such as the relative enhancement of different parts of the line profile or the displacement of the peak of the line. The study of BEL profiles of different ionization in a microlensed QSO image could be an alternative method for probing the BLR structure and size.

Subject headings: cosmology: gravitational lensing — quasars: emission lines

1. INTRODUCTION

The change in the continuum flux of quasars by stars or compact objects in intervening galaxies (gravitational microlensing) is now a well-established observational phenomenon.

¹Instituto de Astrofísica de Canarias, E-38205 La Laguna, Tenerife, Spain

²Astronomical Observatory, Volgina 7, 11160 Belgrade, Serbia, Yugoslavia

Several studies have attempted to resolve the structure of the region generating the optical and UV continuum by using the microlensing effect as a gravitational telescope (see Yonehara 1999, and references therein). However, it has usually been assumed that the size of the region generating the broad emission lines (BELs) of quasars is too large (0.1–1 pc within the framework of the standard model, Rees 1984) to be substantially affected by stellar-mass lenses. According to previous studies (Nemiroff 1988; Schneider & Wambsganss 1990), by comparing one line in different components of a multiple-image quasar, we would be able to detect only fractional deviations of the lensed from the unlensed profile. Even using optimistic estimates for the microlens masses, these deviations would amount to a modest 10–30% range. However, new results concerning the BLR structure and kinematics are relevant to these studies, and could substantially change the common view about the expected influence of microlensing events on the BEL profiles. A recent study (Wandel, Peterson, & Malkan 1999) that compares the BLR size determinations obtained using both the reverberation and the photoionization techniques for a sample of 19 low luminosity AGN (mainly Seyferts) inferred a size in the range of a few light days to a few light weeks. For AGN of greater luminosity (QSOs) Kaspi et al. (2000) derived sizes from the Balmer lines in the range from 13 to 514 light days, finding a global scaling of the BLR size as a function of the intrinsic luminosity, $r_{\text{BLR}} \propto L^{0.7}$.

The purpose of this paper is to revisit the influence of microlensing in the BEL by incorporating these new results. In §2 we estimate the possibility of microlensing on the BLR of different known multiple-image quasars. In §3 we use simple, but not kinematically unrealistic, models of BLRs to study qualitatively the effects that microlensing can produce on the line profiles. In §4 the observational implications and applications will be discussed. Finally, the main conclusions are summarized in §5.

2. ESTIMATES FOR SOME KNOWN SYSTEMS OF MULTIPLE-IMAGE QSOs

Only extended objects of sizes comparable to or smaller than the Einstein radius associated with the gravitational lens will experience appreciable amplifications (e.g., Schneider, Ehlers, & Falco 1992). Thus, in the framework of the AGN standard model where the BLR is supposed to have a radius in the 0.1–1 pc range, only massive deflectors could give rise to significant amplifications. However, recent results from the MACHO project indicate that the most likely microdeflector masses in the Galactic halo are in the range 0.15–0.9 M_{\odot} (Alcock et al. 2000b). In the Galactic bulge the microdeflector masses are in good agreement with normal-mass stars (Alcock et al. 2000a). Estimates from the lightcurve of

Q 2237+0305 (Wyithe, Webster, & Turner 2000) are also in reasonable agreement with these values. Consequently, significant amplifications of the BEL would not be expected according to the standard model. This result has been pointed out by other authors (Nemiroff 1988; Schneider & Wambsganss 1990), even if they were somewhat optimistic concerning the distribution of the microlens mass adopted.

However, recent research on the BEL seems to indicate that the BLR could be substantially smaller than expected in the standard model (Wandel et al. 1999). Based on the idea that ‘the continuum/emission line cross-correlation function measures the responsivity-weighted radius of the BLR (Koratkar & Gaskell, 1991)’, Wandel et al. (1999) have obtained reliable size measurements. The sizes obtained using this technique (reverberation mapping) are consistent with the substantially more extensive but less accurate measurements inferred from the photoionization method. The results summarized by Wandel et al. (1999) exhibited a large scatter (from 1.4 to 107 days) which could be attributed to: i) the different size/structure of the BLR in different objects, and ii) the different sizes of the regions associated with emission lines of different degrees of ionization. The latter possibility has been neatly exemplified in the case of NGC 5548, in which luminosity-weighted radii ranging from ~ 2.5 days for the He II $\lambda 1640$ line to the 28 days corresponding to the [C III] $\lambda 1909$ line have been found (Peterson & Wandel 1999). NGC 5548 and the other objects in the sample of Wandel et al. (1999) are AGN of relatively low luminosity. However, there is a range of luminosities among the lensed QSOs. To take this fact into account we use the results from Kaspi et al. (2000), who found a dependence between the BLR size and the intrinsic luminosity of the AGN, $r_{\text{BLR}} \propto L^{0.7}$.

2.1. Search for candidates

For a typical lens configuration ($z_l = 0.5$ and $z_s = 2$), the projected Einstein radius of the microlens on the source is $\eta_0 \sim 20(M/M_\odot)^{(1/2)}$ light-days (for a $\Omega = 0.3$ flat cosmology and $H_0 = 70 \text{ km s}^{-1} \text{ Mpc}^{-1}$). Objects with $r_{\text{BLR}} \lesssim \eta_0$ are significantly affected by microlensing. So the relevant question is whether in the sample of the ~ 70 known gravitational lens systems there exist some lensed quasars with BLR radius $r_{\text{BLR}} \lesssim \eta_0$. To answer this question we can apply the Kaspi relationship $r_{\text{BLR}} \propto L^{0.7}$ using NGC 5548 as a reference object. We adopt two values for the BLR size of NGC 5548 in order to account for its stratification: 21.2 light-days (Balmer lines, Kaspi et al. 2000) and 2.5 light-days (high ionization, He II line, Peterson & Wandel 1999). One can straightforwardly verify that for a $z = 2$ (1) quasar with $m_V = 24.3$ (22.5) would have the same r_{BLR} as NGC 5548, i.e., the microlensing on the BLR would be quite pronounced. Multiple-image objects of this apparent magnitude can be

detected and, in fact, there are several examples among the currently known gravitational lens systems.

We can refine this rough estimate by taking into account the redshift and apparent magnitude of each lensed object. With this aim, in Figure 1 we show contour plots of the BLR radius as a function of the source redshift and apparent magnitude using both reference values for the BLR of NGC 5548 and the $r_{\text{BLR}} \propto L^{0.7}$ law. We have also included in Fig. 1 the observed redshift–magnitude values corresponding to a sample of 31 QSOs selected from the ~ 70 known gravitational lenses with the criteria of having the lens and source redshifts and the optical magnitude well determined. We have used the V magnitude of the brightest lensed image (in B 1933+507, B 2045+265, MG 0414+0534, PKS 1830-211 and other four unlabeled objects we have inferred V from I using $V - I = 0.50$; in HST 1413+5211 and other unlabeled object we have inferred V from R using $V - R = 0.11$). The data have been mainly obtained from the CASTLES web page (<http://cfa-www.harvard.edu/castles>). For the previous and subsequent calculations we have adopted from NED the visible magnitude and redshift of NGC 5548, $m_V = 13.3$ and $z = 0.017$. To transform apparent magnitudes into intrinsic luminosities we have made use of the equation $L = 4\pi D_{\text{lum}}^2 S(1+z)^{(\alpha-1)}$, which relates the absolute luminosity of the source, the luminosity distance, D_{lum} , the apparent flux, S , and the spectral index, α , defined by $F_\nu \propto \nu^{-\alpha}$. We have considered an $\Omega = 0.3$ flat cosmology and a value for the spectral index $\alpha = 0.5$ (e.g., Richards et al. 2001).

In Fig. 1 we can identify a group of ten systems with magnitude $m_V > 21$ that would lie in the region $R \lesssim 100$ light-days (Balmer lines) and in the region $r \lesssim 10$ light-days (high-ionization lines). These systems are possibly affected by microlensing, with particular strength in the case of the high-ionization lines. However, the observed magnitudes of the lensed QSOs should be corrected by extinction and gravitational lens amplification. The amount of extinction in the gravitational lenses is unknown for most of them, but it can be in the range from dust-free lenses to strongly reddened systems (e.g., Falco et al. 1999; Muñoz et al. 2001 and references therein). We selected the magnitude from the brightest QSO image, which in most of the cases is the less reddened. As a first approximation to the expected amount of obscuration we can adopt the mean extinction, $\langle \Delta m \rangle = 0.6$, derived by Falco, Kochanek, & Muñoz (1998) comparing the statistics of radio and optical lensed quasars. On the other hand, the quasar source is amplified by the gravitational lens and the true luminosity of the unlensed quasar should be calculated by fitting a lens model to each system. The exact amplification of each gravitational lens system depends on the lens model and on the particular configuration of the system, but an average expected amplification between the brightest image and the unlensed source is ~ 1.5 mag (e.g., Lehár et al. 2000). Thus, a roughly averaged correction of the combined effects of extinction and lens amplification can be made by adding ~ 1 mag to the apparent QSO magnitude.

Taking into account the +1 mag shift, the number of possible candidates affected by microlensing (at least in the high-ionization lines) is increased to 12 ($\sim 40\%$ of the sample, see Fig. 1). Our selection procedure could include not only intrinsically low-luminosity but also reddened objects in the list of candidates. As we have seen, a 1 mag shift due to underestimation of the extinction will not substantially modify the set of candidates. This moderates the impact of the extinction uncertainties in the selection of candidates, but we cannot discard the possibility that our statistics were biased by heavily reddened objects of intrinsically high luminosity. This is the case for B 0218+357, which according to the rest-frame $E(B - V) = 1.52$ obtained from Falco et al. (1999) would be an intrinsically high-luminosity object reddened by extinction. MG 0414+0534 is also a very reddened object, but in this case probably owing to a very red intrinsic spectral distribution ($F_\nu \propto \nu^{-9}$ was measured at optical wavelengths by Hewitt et al. 1992). This implies that MG 0414+0534 could have a high intrinsic rest-frame V luminosity but also indicates that this object is probably a radio galaxy rather than a QSO.

The identification of the candidates available in the literature supports the hypothesis that most of them are intrinsically low-luminosity objects, since in most cases the objects cannot be clearly classified as bright QSOs but admit alternative classifications as objects with lower levels of activity (radio galaxies, underluminous QSOs, starburst galaxies, Seyfert 2 galaxies, or other types of AGNs). This also implies that we have probably overestimated the luminosities of the candidate objects because we have not removed the contribution from the galaxy, which is probably far from negligible.

2.2. Estimate of the amplification in B 1600+434

It would be very useful to compute the expected amplifications for each object in the list of candidates. However, lack of knowledge of the extinction in each system and, to some extent, of a precise classification of the source, could affect the results significantly. We have selected the gravitational lens discovered by Jackson et al. (1995), B 1600+434, a double-imaged typical quasar at $z_s = 1.59$, lensed by an edge-on spiral galaxy at $z_l = 0.42$, in which both the lens amplification and the extinction might be reasonably well known. To calculate the amplification induced in B 1600+434 by the lens galaxy we have fitted a singular isothermal ellipsoid (SIE) to this double-imaged quasar. Thus, we obtain an amplification of 0.96 mag for the brightest quasar image, which has an observed V-band magnitude of $m_V = 22.69$. For the extinction we have used the result from Falco et al. (1999), $A_V = 1.02$ mag. From the intrinsic luminosity obtained after correcting for amplification and extinction ($m_V = 22.63$) and using the Kaspi et al. relationship, we have estimated radii of 45 and

5.3 lighth-days for the Balmer and He II BLRs, respectively (according to the two values of reference adopted for NGC 5548).

To estimate the maximum amplification, μ_{\max} , we adopt the expression (e.g., Schneider et al. 1992):

$$\mu_{\max} \sim \frac{\sqrt{\left(\frac{r_{\text{BLR}}}{\eta_0}\right)^2 + 4}}{\left(\frac{r_{\text{BLR}}}{\eta_0}\right)}, \quad (1)$$

where r_{BLR} is the BLR radius, and η_0 is given by

$$\eta_0 = \sqrt{4 \frac{GM}{c^2} \frac{D_s D_{\text{ds}}}{D_d}} \quad (2)$$

(D_d and D_s are the angular diameter distances to the lens and the QSO respectively, and D_{ds} is the angular diameter lens–QSO distance).

If we apply these formulae to B 1600+434, we find that a solar-mass stellar microlens would induce a modest, albeit potentially observable, amplification of 1.4 in the Balmer lines and a strong amplification of 8.2 in He II. A $0.1 M_{\odot}$ microlens would also induce an appreciable amplification of 2.76 in the He II lines. We do not calculate the amplification by microlensing on the BEL for the other objects in the list because the exact amount of extinction is unknown for most of them, and because we can no longer suppose that the $F_{\nu} \propto \nu^{-0.5}$ dependence of the energy distribution is a realistic approach for some of the objects.

In summary, although most of the lensed quasars ($\gtrsim 70\%$ of the total) are intrinsically high-luminosity quasars (so that no strong microlensing in the BEL is expected) we found that $\lesssim 30\%$ of the lensed sources are faint enough to be considered as possibly affected by microlensing in the BEL.

3. MICROLENSING EFFECTS ON THE PROFILE OF THE BROAD EMISSION LINES

When an organized velocity field governs the kinematics of the BLR, microlensing can give rise to a selective amplification of the emission-line profile (Nemiroff 1988). The shape of the line depends on the location of the source with respect to the optical axis (defined by the observer and the microlens) and can change with the relative movement between the microlens and the BLR. In this section we adopt the kinematic models for the BLR used by Robinson (1995) to study the range of profile shapes that exists among AGN in the context of a simple parameterization of some basic properties of the BLR such as emissivity and

velocity law. Our intention is to study, in this framework, the effects induced in the line profile by a microlens in different locations with respect to the center of the BLR.

We assume that a single microdeflector is affecting the BLR. This supposition adequately serves the objectives of the present paper (a more realistic approach based on the existence of a random distribution of microdeflectors will be analyzed in a future paper).

In accordance with Robinson (1995), we consider three different geometries (spherical, biconical, and cylindrical) and adopt the following radial dependences for the emissivity and magnitude of the velocity:

$$\epsilon(r) = \epsilon_0 \left(\frac{r}{r_{\text{in}}} \right)^\beta \quad (3)$$

and

$$v(r) = v_0 \left(\frac{r}{r_{\text{in}}} \right)^p. \quad (4)$$

We compute the emission-line profile from the expression

$$F_\lambda = \int_V \epsilon(r) \delta \left[\lambda - \lambda_0 \left(1 + \frac{v_{\parallel}}{c} \right) \right] \mu(\vec{r}) dV, \quad (5)$$

where

$$\mu(\vec{r}) = \frac{u^2 + 2}{u\sqrt{u^2 + 4}} \left(u = \frac{|\vec{r} - \vec{r}_0|}{\eta_0} \right) \quad (6)$$

is the amplification associated with the microlens, $\vec{r}_0 \sim (r_0, \varphi_0)$ is the position of the microlens, η_0 is the Einstein radius, and v_{\parallel} is the projected line-of-sight velocity.

We adopt inner (r_{in}) and outer (r_{BLR}) radii for the BLR.

It is convenient to scale the distances to the Einstein radius associated with the microlens. In this way, the relevance of the microlens effect can be characterized by the quantity

$$\tilde{r}_{\text{BLR}} = \frac{r_{\text{BLR}}}{\eta_0}. \quad (7)$$

We consider two values (1 and 4) for \tilde{r}_{BLR} . We assume throughout that $r_{\text{in}} = 0.1 r_{\text{BLR}}$.

To study the effects produced by the relative off-centering between the microlens and the BLR, we compute line profiles corresponding to a grid of displacements of the microlens relative to the center of the BLR. We consider 25 positions in the positive XY quadrant ranging from 0 to \tilde{r}_{BLR} in both the X and Y axes (Fig. 2).

In the Appendix we collect all the formal development and formulae and concentrate on the results in the following sections.

3.1. SPHERICAL SHELL

In the case of a spherical ensemble of emitters flowing radially, the projected line-of-sight velocity corresponding to an emitter at a position (r, θ) is given by

$$v_{||} = v_0 \left(\frac{r}{r_{\text{in}}} \right)^p \cos \theta \quad (p > 0). \quad (8)$$

We have used the same notation as Robinson (1995) for the parameters related to the relative velocity,

$$x = \frac{\lambda - \lambda_0}{\lambda_0} \frac{c}{v_{\text{max}}}, \quad (9)$$

and we will refer to the line parameter which defines the line shape:

$$\eta = \frac{\beta + 3}{p} - 1. \quad (10)$$

The line profile (see Appendix A.1) is obtained by integrating

$$F_x = \begin{cases} \frac{\epsilon_0 r_{\text{int}}^2 c}{\lambda_0 v_0} \int_0^{2\pi} \int_{\text{Max}[r_{\text{in}}, r_{\text{lim}}]}^{r_{\text{BLR}}} \left(\frac{r}{r_{\text{in}}} \right)^{\beta+2-p} [\mu(x, r, \varphi)]_{f=0} dr d\varphi & r_{\text{lim}} < r_{\text{BLR}} \\ 0 & r_{\text{lim}} > r_{\text{BLR}} \end{cases} \quad (11)$$

where $r_{\text{lim}} = r_{\text{in}} (x/x_m)^{1/p}$, $x_m = v_0/v_{\text{max}} = (r_{\text{in}}/r_{\text{BLR}})^p$, and $[\mu(x, r, \varphi)]_{f=0}$ is given by Eq. 6, inserting Eq. A8 into Eq. A10.

Following Robinson (1995), we take η as the parameter defining the emission-line profile. For the spherical case we consider two values, a) $\eta = 2$ and b) $\eta = -0.25$, which in absence of microlensing would correspond to concave and convex profile wings, respectively. In absence of microlensing, only this parameter is needed to characterize the line profile. In the presence of microlensing we need also to fix another parameter. We select the emissivity exponent $\beta = -1.5$ (see Eq. 3). The exponent of the velocity law, p , is then obtained from Equation 10. Thus, for case a) we have $p = 0.5$ and for case b) $p = 2$.

In Figs. 3, 4 we present the grids of profiles for $\tilde{r}_{\text{BLR}} = 1, 4$ for case a) and in Figs. 5, 6 for case b). The influence of microlensing on the line profiles would be observable when the microlens is centered on the BLR, and also in many other cases in which the microlens is off-centered. The displacement of a microlens across the BLR would induce changes in the relative strength of different parts of the line profile, relatively enhancing the wings when the microlens is centered on the BLR and the core when it is sited in the outer parts. However, no relative enhancements between the blue and red parts of the profile would appear due to the high symmetry of the spherical model.

As mentioned previously, one notable property of Robinson’s models is that the profile shape depends only on η . This implies that from the study of the line profile it is not possible to derive direct information on the velocity field or the emissivity law. Could the presence of microlensing break this degeneracy for a spherical shell? Such questions as the existence of a monotonically increasing or decreasing dependence with radial distance of the velocity field may have a formal answer. In principle, it would be possible to invert the line-profile expression (Eq. 11) obtained for several different positions of the microlens to recuperate, making suitable suppositions, the law for radial velocities. However, it is not easy to decide on direct observational criteria to carry out this study.

To illustrate the difficulties in deriving information from the microlensed line profile in the spherical case, notice that not even a simple question like the existence of outflow or inflow can be answered. (For the spherical case there is always the same contribution of receding and approaching emitters along the line of sight which would undergo the same magnification.)

3.2. BICONICAL SHELL

Much observational evidence (Zheng, Binette, & Sulentic 1990; Marziani, Calvani, & Sulentic 1992) and theoretical work supports the idea that the flow of emitting gas is anisotropic, preferentially confined to a pair of oppositely directed cones. In this model we need three polar coordinates (r, θ, φ) measured with respect to the cone axis to express the projected line-of-sight velocity corresponding to an emitter,

$$v_{||} = v_0 \left(\frac{r}{r_{\text{in}}} \right)^p \xi \quad (p > 0), \quad (12a)$$

$$\xi = \sin \theta \sin \varphi \sin i + \cos \theta \cos i, \quad (12b)$$

where i is the inclination of the cones axis with respect to the line of sight.

This model can give rise to a variety of line profiles (see Figure 5 of Robinson 1995). We are going to consider the two limiting cases: $i = 0^\circ$ and $i = 90^\circ$. We will adopt the cone half-angle $\theta_c = 30^\circ$, and $\beta = -1.5$.

3.2.1. $i = 0^\circ$

The line profile (see Appendix A.2.1) is obtained by integrating

$$F_x = \begin{cases} \frac{\epsilon_0 r_{\text{in}}^2 c}{\lambda_0 v_0} \int_0^{2\pi} \int_{\text{Max}[r_{\text{lim}}, r_{\text{in}}]}^{\text{Min}[r_{\text{sup}}, r_{\text{BLR}}]} \left(\frac{r}{r_{\text{in}}}\right)^{\beta+2-p} [\mu(x, r, \varphi)]_{f=0} dr d\varphi & (r_{\text{lim}} < r_{\text{BLR}} \text{ and } r_{\text{sup}} > r_{\text{in}}) \\ 0 & \text{in the other cases} \end{cases} \quad (13)$$

where $r_{\text{lim}} = r_{\text{in}} (|x|/x_m)^{1/p}$, $r_{\text{sup}} = r_{\text{BLR}} (|x|/\cos\theta_c)^{1/p}$, and $[\mu(x, r, \varphi)]_{f=0}$ is given by Eq. 6, inserting Eq. A8 into Eq. A10, with $x_m = v_0/v_{\text{max}} = (r_{\text{in}}/r_{\text{BLR}})^p$.

In Figs. 7, 8 we present the grids of profiles for $\tilde{r}_{\text{BLR}} = 1, 4$ corresponding to $\eta = 2$, and in Figs. 9, 10 the grids corresponding to $\eta = -0.25$. In both cases we obtain two-peaked profiles. As in the case of the sphere, the influence of microlensing when the microdeflector is centered with the BLR is very noticeable. However, in the biconical case, the change in the relative enhancements of different parts of the line profile caused by the displacement of the microlens with respect to the center of the BLR is more noticeable than in the spherical one.

3.2.2. $i = 90^\circ$

The line profile (see Appendix A.2.2) is obtained by integrating

$$F_x = \int_{\text{Max}[r_{\text{lim}}, r_{\text{in}}]}^{r_{\text{BLR}}} \left(\left[\int_{\theta_{\text{lim}}}^{\theta_c} + \int_{\pi-\theta_c}^{\text{Min}[\pi-\theta_{\text{lim}}, \pi]} \right] f(x, r, \theta) d\theta \right) dr, \quad (14)$$

where

$$f(x, r, \theta) = \begin{cases} \frac{\epsilon_0 r_{\text{in}}^2 c}{\lambda_0 v_0} \left(\frac{r}{r_{\text{in}}}\right)^{\beta+2-p} \frac{\sin\theta [\mu_+(x, r, \theta) + \mu_-(x, r, \theta)]_{f=0}}{\sqrt{\sin^2\theta - \left[\frac{x}{x_m} \left(\frac{r}{r_{\text{in}}}\right)^{-p}\right]^2}} & (\theta > \theta_{\text{lim}}), \\ 0 & \text{in other cases,} \end{cases} \quad (15)$$

with $\theta_{\text{lim}} = \arcsin[(|x|/x_m)(r/r_{\text{in}})^{-p}]$, $x_m = v_0/v_{\text{max}} = (r_{\text{in}}/r_{\text{BLR}})^p$, and $[\mu_{\pm}(x, r, \theta)]_{f=0}$ is given by Eq. 6, inserting Eq. A20 into Eq. A22.

In Figs. 11, 12 we present the grids of profiles for $\tilde{r}_{\text{BLR}} = 1, 4$ corresponding to $\eta = 2$ and in Figs. 13, 14 the grids corresponding to $\eta = -0.25$. In this case, $i = 90^\circ$, we obtain single-peaked profiles, convex for $\eta = 2$, and concave for $\eta = -0.25$. The effects of microlensing are very strong, even for the case $\eta_0 = r_{\text{BLR}}/4$ (Figs. 12 and 14).

For the limiting geometries considered here ($i = 0^\circ, 90^\circ$) there are no asymmetries induced by the microlensing in the line profile. However, for an arbitrary inclination, an off-centered microlens should induce relative enhancements of the blue and red parts. Due to the loss of symmetry of the projected velocity field with respect to that of the spherical case, the inversion of the profile equation to study the velocity field should be easier. For instance, in the case of small cone aperture, the crossing of a microlens along the biconical axis would serve to virtually map the radial dependence of the velocity field.

3.3. CYLINDRICAL SHELL

Rotation in a plane disk has been often considered in relation to the kinematics of the BLR and is typically characterized by the presence of a central dip (Mathews 1982) in the line profile arising from the finite extension of the outer radius of the disk. This feature is not usually found in the observed line profiles, but there are several ways to avoid it in the models (see Robinson 1995). Nevertheless, the existence of rotation is strongly supported by recent observational work (Peterson & Wandel 1999).

3.3.1. Keplerian disk

The Keplerian disk is a particular case of the cylindrical disk with velocity field,

$$v_{\parallel} = v_0 \left(\frac{r}{r_{\text{in}}} \right)^p \cos \varphi \sin i \quad (p = -0.5), \quad (16)$$

where r and φ are polar coordinates of an emitter in the disk.

The line profile is given by (see Appendix A.3.1):

$$F_x = \begin{cases} \frac{\epsilon_0 r_{\text{in}} c}{\lambda_0 v_0 \sin i} \int_{r_{\text{in}}}^{\text{Min}[r_{\text{lim}}, r_{\text{BLR}}]} \left(\frac{r}{r_{\text{in}}} \right)^{\beta+1-p} \frac{[\mu_+(x,r) + \mu_-(x,r)]_{f=0}}{\sqrt{1 - \left[\frac{x}{\sin i} \left(\frac{r}{r_{\text{in}}} \right)^{-p} \right]^2}} dr & (r_{\text{lim}} > r_{\text{in}}) \\ 0 & (r_{\text{lim}} < r_{\text{in}}) \end{cases} \quad (17)$$

where $r_{\text{lim}} = r_{\text{in}} (|x|/\sin i)^{1/p}$, $x_{\text{in}} = (r_{\text{in}}/r_{\text{BLR}})^{-p}$ and $[\mu_{\pm}(x, r)]_{f=0}$ is given by Eq. 6, inserting Eqs. A27 and A28 into Eq. A30.

In Figs. 15, 16 we present the grid of profiles for $\tilde{r}_{\text{BLR}} = 1, 4$ with $i = 45^\circ$, $\beta = -1.5$, and $\eta = (\beta + 2)/p - 1$. The most noticeable feature associated with the Keplerian case (and with the cylindrical case in general) is the presence of strong asymmetries in the line profiles induced by the microlensing.

3.3.2. Modified Keplerian disk

An easy way of generating a single-peaked profile in the cylindrical case is to modify the velocity field increasing the contribution of low velocities. For our purpose we will adopt

$$v_{\parallel} = v(r) \cos \varphi \sin i \quad (p = -0.5) \quad (18a)$$

and

$$v(r) = v_0 \left(\frac{\frac{1}{r} - \frac{1}{r_{\text{BLR}}}}{\frac{1}{r_{\text{in}}} - \frac{1}{r_{\text{BLR}}}} \right)^{-p} = v_0 u(r), \quad (18b)$$

where r and φ are polar coordinates of an emitter in the disk.

In this case, the line profile is given by (see Appendix A.3.2),

$$F_x = \begin{cases} \frac{\epsilon_0 r_{\text{in}} c}{\lambda_0 v_0 \sin i} \int_{r_{\text{in}}}^{\text{Min}[r_{\text{lim}}, r_{\text{BLR}}]} \left(\frac{r}{r_{\text{in}}} \right)^{\beta+1} \frac{[\mu_+(x,r) + \mu_-(x,r)]_{f=0}}{u(r) \sqrt{1 - \left(\frac{x}{u(r) \sin i} \right)^2}} dr & (r_{\text{lim}} > r_{\text{in}}) \\ 0 & (r_{\text{lim}} < r_{\text{in}}) \end{cases} \quad (19)$$

where $r_{\text{lim}} = \left[(|x|/\sin i)^{-1/p} (1/r_{\text{in}} - 1/r_{\text{BLR}}) + 1/r_{\text{BLR}} \right]^{-1}$, $x_{\text{m}} = r_{\text{in}}/r_{\text{BLR}}$, and $[\mu_{\pm}(x, r)]_{f=0}$ is given by Eq. 6, inserting Eqs. A27 and A28 into Eq. A30.

In Figs. 17, 18 we present the grid of profiles for $\tilde{r}_{\text{BLR}} = 1, 4$ with $i = 45^\circ$ and $\beta = -1.5$. In addition to the asymmetries, the most interesting effect of microlensing on the line profiles corresponding to the Keplerian modified velocity field is the displacement of the line peak with respect to the centroid of the non-microlensed line profile, Δx_{p} , (Fig. 19), which, independently of the mass considered ($\tilde{r}_{\text{BLR}} = 1, 4$), can be of the order of as much as $\sim \text{FWZI}/4$.

4. DISCUSSION

If the models and assumptions of the previous sections constitute a good description of BLR microlensing, we could conclude that the effects of this phenomenon on the line profiles should be not only noticeable but also easily detectable in some lens systems.

The experimental situation, however, is more complex. In first place, the BELs are blended with the narrow emission lines, which come from the much more extended narrow-line region (NLR), which would be not affected by microlensing. In fact, it is likely that diverse transition regions between the BLR and the NLR could also contribute to the core of the line profile. Second, the compactness of the lens systems makes observation very difficult.

For instance, in the case (B 1600+434) in which we have obtained a realistic estimate for microlensing amplification there are two compact images, the lens galaxy (an edge-on spiral), and some additional extended emission, all within a separation of $\sim 2''$. This is a major setback when trying to obtain individual spectra, and only modern spectroscopic techniques (2D spectroscopy, Mediavilla et al. 1998 and references therein) or observation from space avoid the problems induced by source blending and differential atmospheric refraction. In any case, to detect microlensing we should obtain spectra (preferably of high-ionization lines) with a high S/N ratio in the wings of the line profile, where the contribution from the BLR would be dominant.

The emissivity is another important parameter that can affect the detection of microlensing in BELs. In Fig. 20 we present the ratio of the amplified to unamplified line profiles corresponding to the modified Keplerian case, where we have changed the emissivity parameter, β . For a highly concentrated BLR ($\beta = -4$) the effect is stronger when the BLR is almost centered on the microlens and weak for larger displacements of the microlens with respect to the center of the BLR. But when the emissivity is constant (for a disk of uniform brightness, $\beta = 0$) the effects of microlensing remain noticeable for all displacements considered and are hence more likely to be observed.

In Fig. 1 we have labeled the gravitational lens systems in which significant BEL microlensing could be detected (30% of the total). However, in other systems a modest effect could be detectable by looking at high-ionization lines. This is important because other questions than the amplification, such as the crossing time of the microlens across the BLR or the frequency of the events, can lead us to study a gravitational lens system in particular. For instance, in a favorable case it would be possible not only to compare the line profile corresponding to microlensed and non-microlensed images but also to observe in the line profile of an image changes attributable to the microlens crossing. In the most favorable case from this perspective, Q 2237+0305, microlensing events are reported each year with crossing times of the order of a year or less. However, this is a bright QSO in which only very modest amplifications of 30% or less can be expected in the high-ionization lines. This estimation of the amplification is, in any case, subject to changes in the BLR-size vs QSO-luminosity relationship, and also to the expected intrinsic dispersion from object to object.

In spite of the last comment, the amplifications associated with the high-ionization lines could be high in many cases, and only a strong departure from the assumptions made in this study (e.g., a severe underestimate of the extinction, very different behavior of the BLR-size/QSO-magnitude relationship, or an unexpectedly low-mass population of microlenses) could avoid the detection of microlensing in the BELs by comparing the high-ionization line

profiles of a microlensed and a non-microlensed image in the most favorable cases. According to this, the study of the incidence of microlensing in BELs could become a tool for studying the BLR size and stratification, especially when lines of different ionization are observed.

5. CONCLUSIONS

In the light of recent discoveries concerning the BLR size and its scaling with AGN luminosity, currently accepted values for microlens masses, and a variety of kinematic models for the BLR, we have revisited the influence of microlensing in the BEL. We have computed grids of line profiles corresponding to different displacements of the microlens with respect to the BLR center. Some results are worth summarizing:

1.- The global amplification of the BEL induced by microlensing events could be relevant. We identify a group of ten gravitational lens systems (about 30% of the total sample) for which the microlensing effect could be observable, especially in high-ionization lines. In other gravitational lenses the microlensing amplifications would be much more modest.

2.- Even for relatively small microlenses corresponding to high values of the BLR radius/Einstein radius quotient, ($r_{\text{BLR}}/\eta_0 \sim 4$), the effects produced by the differential amplification of the line profile (relative enhancement of different parts of the line profile, line asymmetries, displacement of the peak of the line, etc.) would be easily detectable except for highly symmetric velocity fields. The displacement of the peak of the line profile caused by microlensing is especially interesting, since it could otherwise induce inexplicable redshift differences between the different images in a gravitational lens system.

3.- The study of the changes between the BEL profiles corresponding to microlensed and non-microlensed images, or among the BEL profiles of lines with different ionization in a microlensed image could be useful for probing current ideas about BLR size and stratification.

We would like to acknowledge valuable and useful comments of the anonymous referee. This work was supported by the P6/88 project of the Instituto de Astrofísica de Canarias (IAC). L. Č. P. is supported by Ministry of Science, Technologies and Development of Serbia through the project ‘Spectroscopy of Extragalactic Objects’.

A. MODELING THE BROAD LINE REGION

Nowadays, there is no generally accepted model for the geometry and dynamics of the broad line region. So, we adopt in this paper the discrete cloud model (see Robinson 1995) in which it is assumed that the magnitude of the velocity and the volume emissivity may be independently specified by a power law. It is also assumed that the clouds or volume elements emit line radiation isotropically.

The amplified line profile produced by the system is obtained from:

$$F_\lambda = \int_V \epsilon(r) \delta \left[\lambda - \lambda_0 \left(1 + \frac{v_{||}}{c} \right) \right] \mu(\vec{r}) dV, \quad (\text{A1})$$

where the integral is taken over the total volume occupied by the clouds, $\mu(\vec{r})$ is the relative amplification that the microlens produces over the line profile, and $v_{||}$ is the projection of the velocity field along the line of the sight. Finally, $\epsilon(r)$ is the volume emissivity of the clouds:

$$\epsilon(r) = \epsilon_0 \left(\frac{r}{r_{\text{in}}} \right)^\beta, \quad (\text{A2})$$

r_{in} being the inner radius of the cloud system.

The geometry of the BLR is unknown, but it seems plausible that its overall structure could be characterized by one of three basic symmetries: spherical, conical, or cylindrical.

A.1. SPHERICAL SHELL

Let us first consider a spherically symmetric cloud ensemble of outer radius r_{BLR} , which is characterized by a radial velocity field. The component of the velocity parallel to the line of sight is:

$$v_{||} = v_0 \left(\frac{r}{r_{\text{in}}} \right)^p \cos \theta \quad (p > 0). \quad (\text{A3})$$

If the microlens is placed at $\vec{r}_0 \sim (r_0, \varphi_0)$ and the Einstein radius is η_0 , the relative amplification is given by (e.g., Schneider et al. 1992):

$$\mu(\vec{r}) = \frac{u^2 + 2}{u\sqrt{u^2 + 4}}, \quad u = \frac{|\vec{r} - \vec{r}_0|}{\eta_0}, \quad (\text{A4a})$$

$$|\vec{r} - \vec{r}_0| = \sqrt{(r \sin \theta \cos \varphi - r_0 \cos \varphi_0)^2 + (r \sin \theta \sin \varphi - r_0 \sin \varphi_0)^2}. \quad (\text{A4b})$$

To compute the integral in Eq. A1, we define:

$$f \equiv \lambda - \lambda_0 \left[1 + \frac{v_0}{c} \left(\frac{r}{r_{\text{in}}} \right)^p \cos \theta \right]. \quad (\text{A5})$$

Equation A1, when the integral in the θ dimension is done and the parameters $x = c(\lambda - \lambda_0)/(v_{\text{max}}\lambda_0)$ and $x_m = v_0/v_{\text{max}} = (r_{\text{in}}/r_{\text{BLR}})^p$ are defined, appears as:

$$F_x = \begin{cases} \int_0^{2\pi} \int_{\text{Max}[r_{\text{lim}}, r_{\text{in}}]}^{r_{\text{BLR}}} \epsilon(r) r^2 \frac{[\mu(x, \vec{r})]_{f=0}}{[\frac{df}{d\theta}]_{f=0}} [\sin \theta]_{f=0} dr d\varphi & (r_{\text{lim}} < r_{\text{BLR}}) \\ 0 & (r_{\text{lim}} > r_{\text{BLR}}) \end{cases} \quad (\text{A6})$$

with

$$[\cos \theta]_{f=0} = \frac{x}{x_m} \left(\frac{r}{r_{\text{in}}} \right)^{-p}, \quad (\text{A7})$$

$$[\sin \theta]_{f=0} = +\sqrt{1 - [\cos \theta]_{f=0}^2}, \quad (\text{A8})$$

and

$$\left[\frac{df}{d\theta} \right]_{f=0} = \lambda_0 \frac{v_0}{c} \left(\frac{r}{r_{\text{in}}} \right)^p [\sin \theta]_{f=0}, \quad (\text{A9})$$

where $[\mu(x, \vec{r})]_{f=0}$ is given by Eq. A4a, inserting Eq. A8 into Eq. A4b as:

$$|\vec{r} - \vec{r}_0|_{\pm, f=0} = \sqrt{(r[\sin \theta]_{f=0} \cos \varphi - r_0 \cos \varphi_0)^2 + (r[\sin \theta]_{f=0} \sin \varphi - r_0 \sin \varphi_0)^2}, \quad (\text{A10})$$

and $r_{\text{lim}} = r_{\text{in}} (|x|/x_m)^{1/p}$. The expression of r_{lim} is obtained from the delta condition.

A.2. BICONICAL SHELL

In this case, the broad lines are emitted by a bipolar flow in which clouds moving radially outwards are confined to a pair of oppositely directed cones, whose common axis passes through the optical axis. In general, an individual cloud measured with respect to the cone axis has a projected velocity:

$$v_{\parallel} = v_0 \left(\frac{r}{r_{\text{in}}} \right)^p \xi \quad (p > 0), \quad (\text{A11a})$$

$$\xi = \sin \theta \sin \varphi \sin i + \cos \theta \cos i, \quad (\text{A11b})$$

where i represents the inclination of the axis with respect to the line of sight. For this system, the amplified line profile is:

$$F_{\lambda} = \int_0^{2\pi} \int_{r_1}^{r_2} \left[\int_0^{\theta_c} + \int_{\pi-\theta_c}^{\pi} \right] \epsilon(r) \delta \left[\lambda - \lambda_0 \left(1 + \frac{v_{\parallel}}{c} \right) \right] \mu(\vec{r}) r^2 \sin \theta d\theta dr d\varphi, \quad (\text{A12})$$

where the amplification is given by Eq. A4a, with:

$$|\vec{r} - \vec{r}_0| = \sqrt{(r \sin \theta \cos \varphi - r_0 \cos \varphi_0)^2 + (r \sin \theta \sin \varphi \cos i - r \cos \theta \sin i - r_0 \sin \varphi_0)^2}. \quad (\text{A13})$$

A.2.1. $i = 0^\circ$ CASE

The $i = 0^\circ$ case leads to the amplified line profile:

$$F_x = \begin{cases} \int_0^{2\pi} \int_{\text{Max}[r_{\text{lim}}, r_{\text{in}}]}^{\text{Min}[r_{\text{sup}}, r_{\text{BLR}}]} \epsilon(r) r^2 \frac{[\mu(x, \vec{r})]_{f=0}}{[df/d\theta]_{f=0}} [\sin \theta]_{f=0} dr d\varphi & (r_{\text{lim}} < r_{\text{BLR}} \text{ and } r_{\text{sup}} > r_{\text{in}}), \\ 0 & \text{in the other cases,} \end{cases} \quad (\text{A14})$$

where $[\sin \theta]_{f=0}$ and $[df/d\theta]_{f=0}$ are given by Eqs. A8 and A9, $[\mu(x, \vec{r})]_{f=0}$ is given by Eq. A4a, inserting Eq. A8 into Eq. A10, with $r_{\text{lim}} = r_{\text{in}} (|x|/x_m)^{1/p}$, and $r_{\text{sup}} = r_{\text{BLR}} (|x|/\cos \theta_c)^{1/p}$. The expressions of r_{lim} and r_{sup} can be inferred from delta conditions.

A.2.2. $i = 90^\circ$ CASE

In the $i = 90^\circ$ case we consider a projected velocity of

$$v_{||} = v_0 \left(\frac{r}{r_{\text{in}}} \right)^p \sin \theta \sin \varphi \quad (p > 0). \quad (\text{A15})$$

Let us now define f as:

$$f \equiv \lambda - \lambda_0 \left[1 + \frac{v_0}{c} \left(\frac{r}{r_{\text{in}}} \right)^p \sin \theta \sin \varphi \right], \quad (\text{A16})$$

and then, after integrating in the φ dimension and adopting that $x = c (\lambda - \lambda_0)/(v_{\text{max}} \lambda_0)$ and $x_m = v_0/v_{\text{max}} = (r_{\text{in}}/r_{\text{BLR}})^p$, Eq. A12 becomes:

$$F_x = \int_{\text{Max}[r_{\text{lim}}, r_{\text{in}}]}^{r_{\text{BLR}}} \left(\left[\int_{\theta_{\text{lim}}}^{\theta_c} + \int_{\pi - \theta_c}^{\text{Min}[\pi - \theta_{\text{lim}}, \pi]} \right] f(x, r, \theta) d\theta \right) dr, \quad (\text{A17})$$

where

$$f(x, r, \theta) = \begin{cases} \epsilon(r) r^2 \sin \theta \frac{[\mu_+(x, \vec{r}) + \mu_-(x, \vec{r})]_{f=0}}{[d\mu/d\varphi]_{f=0}}, & (\theta > \theta_{\text{lim}}) \\ 0 & \text{in other cases} \end{cases} \quad (\text{A18})$$

with $\theta_{\text{lim}} = \arcsin[(|x|/x_m)(r/r_{\text{in}})^{-p}]$. The expression of θ_{lim} is inferred from delta conditions. Moreover,

$$[\sin \varphi]_{f=0} = \frac{x}{x_m} \left(\frac{r}{r_{\text{in}}} \right)^{-p} \frac{1}{\sin \theta}, \quad (\text{A19})$$

$$[\cos \varphi]_{\pm, f=0} = \pm \sqrt{1 - [\sin \varphi]_{f=0}^2}, \quad (\text{A20})$$

and

$$\left[\frac{df}{d\varphi} \right]_{\pm, f=0} = -\lambda_0 \frac{v_0}{c} \left(\frac{r}{r_{\text{in}}} \right)^p \sin \theta [\cos \varphi]_{\pm, f=0}. \quad (\text{A21})$$

$[\mu_{\pm}(x, \vec{r})]_{f=0}$ is given by Eq. A4a, inserting Eq. A20 into Eq. A13 as

$$|\vec{r} - \vec{r}_0|_{\pm, f=0} = \sqrt{(r \sin \theta [\cos \varphi]_{\pm, f=0} - r_0 \cos \varphi_0)^2 + (r \cos \theta + r_0 \sin \varphi_0)^2}. \quad (\text{A22})$$

A.3. CYLINDRICAL SHELL

The simplest example of cylindrical symmetry is a plane, i.e., a thin disk. We will suppose that this disk has uniform thickness, $h \ll r_{\text{in}}$, and that the angle between its axis and the line of sight is i . Finally, any point in the disk is assumed to follow a circular orbit about the axis, thus giving a line-of-sight velocity of:

$$v_{\parallel} = v(r) \cos \varphi \sin i, \quad (\text{A23})$$

where r and φ are polar coordinates of an emitter in the disk.

For this system, the amplified line profile is

$$F_{\lambda} = \int_S \epsilon(r) \delta \left[\lambda - \lambda_0 \left(1 + \frac{v_{\parallel}}{c} \right) \right] \mu(\vec{r}) dS. \quad (\text{A24})$$

Let us now define f as:

$$f \equiv \lambda - \lambda_0 \left[1 + \frac{v(r) \cos \varphi \sin i}{c} \right], \quad (\text{A25})$$

and $x = c (\lambda - \lambda_0) / (v_{\text{max}} \lambda_0)$, with $v_0 = v_{\text{max}}$. Then, when the integral in the φ dimension is done, Eq. A24 becomes:

$$F_x = \begin{cases} \int_{r_{\text{in}}}^{\text{Min}[r_{\text{lim}}, r_{\text{BLR}}]} \epsilon(r) r \frac{[\mu_{+}(x, \vec{r}) + \mu_{-}(x, \vec{r})]_{f=0}}{[\frac{df}{d\varphi}]_{+, f=0}} dr & (r_{\text{lim}} > r_{\text{in}}) \\ 0 & (r_{\text{lim}} < r_{\text{in}}) \end{cases} \quad (\text{A26})$$

where

$$[\cos \varphi]_{f=0} = x \frac{v_0}{v(r) \sin i}, \quad (\text{A27})$$

$$[\sin \varphi]_{\pm, f=0} = \pm \sqrt{1 - [\cos \varphi]_{f=0}^2}, \quad (\text{A28})$$

and

$$\left[\frac{df}{d\varphi} \right]_{\pm, f=0} = \lambda_0 \frac{v(r) \sin i}{c} [\sin \varphi]_{\pm, f=0}. \quad (\text{A29})$$

$[\mu_{\pm}(x, \vec{r})]_{f=0}$ is given by Eq. A4a, inserting the expressions of $[\cos \varphi]_{f=0}$ and $[\sin \varphi]_{f=0}$ (Eqs. A27 and A28) into:

$$|\vec{r} - \vec{r}_0|_{\pm, f=0} = \sqrt{(r[\cos \varphi]_{f=0} \cos i - r_0 \cos \varphi_0)^2 + (r[\sin \varphi]_{\pm, f=0} - r_0 \sin \varphi_0)^2}, \quad (\text{A30})$$

and r_{lim} is defined by the condition:

$$v(r_{\text{lim}}) = v_0 \frac{|x|}{\sin i}. \quad (\text{A31})$$

REFERENCES

- Alcock, C. et al. 2000a, *ApJ*, 541, 734
- Alcock, C. et al. 2000b, *ApJ*, 542, 281
- Falco, E. E., Kochanek, C. S., & Muñoz, J. A. 1998, *ApJ*, 494, 47
- Falco, E. E. et al. 1999, *ApJ*, 523, 617
- Hewitt, J. N., Turner, E. L., Lawrence, C. R., Schneider, D. P., & Brody, J. P. 1992, *AJ*, 104, 968
- Jackson, N. et al. 1995, *MNRAS*, 274, L25
- Kaspi, S. et al. 2000, *ApJ*, 533, 631
- Koratkar, A. P., & Gaskell, C. M. 1991, *ApJS*, 75, 719
- Lehár, J. et al. 2000, *ApJ*, 536, 584
- Marziani, P., Calvani, M., & Sulentic, J. W. 1992, *ApJ*, 393, 658
- Mathews, W. G. 1982, *ApJ*, 258, 425
- Mediavilla, E. et al. 1998, *ApJ*, 503, L27
- Muñoz, J. A. et al. 2001, *ApJ*, 563, L107
- Nemiroff, R. 1988, *ApJ*, 335, 593
- Peterson, B. M., & Wandel, A. 1999, *ApJ*, 521, L95
- Rees, M. J. 1984, *ARA&A*, 22, 471
- Richards, G. T. et al. 2001, *AJ*, 121, 2308
- Robinson, A. 1995, *MNRAS*, 272, 647
- Schneider, P., Ehlers, J., & Falco, E. 1992, *Gravitational Lenses* (Berlin: Springer)
- Schneider, P., & Wambsganss, J. 1990, *ARA&A*, 273, 42
- Wandel, A., Peterson, B. M., & Malkan, M. A. 1999, *ApJ*, 526, 579
- Wyithe, J. S. B., Webster, R. L., & Turner, E. L. 2000, *MNRAS*, 315, 51

Yonehara, A., Mineshige, S., Fukue, J., Umemura, M., & Turner, E. L. 1999, *A&A*, 343, 41

Zheng, W., Binette, M., & Sulentic, J. W. 1990, *ApJ*, 365, 115

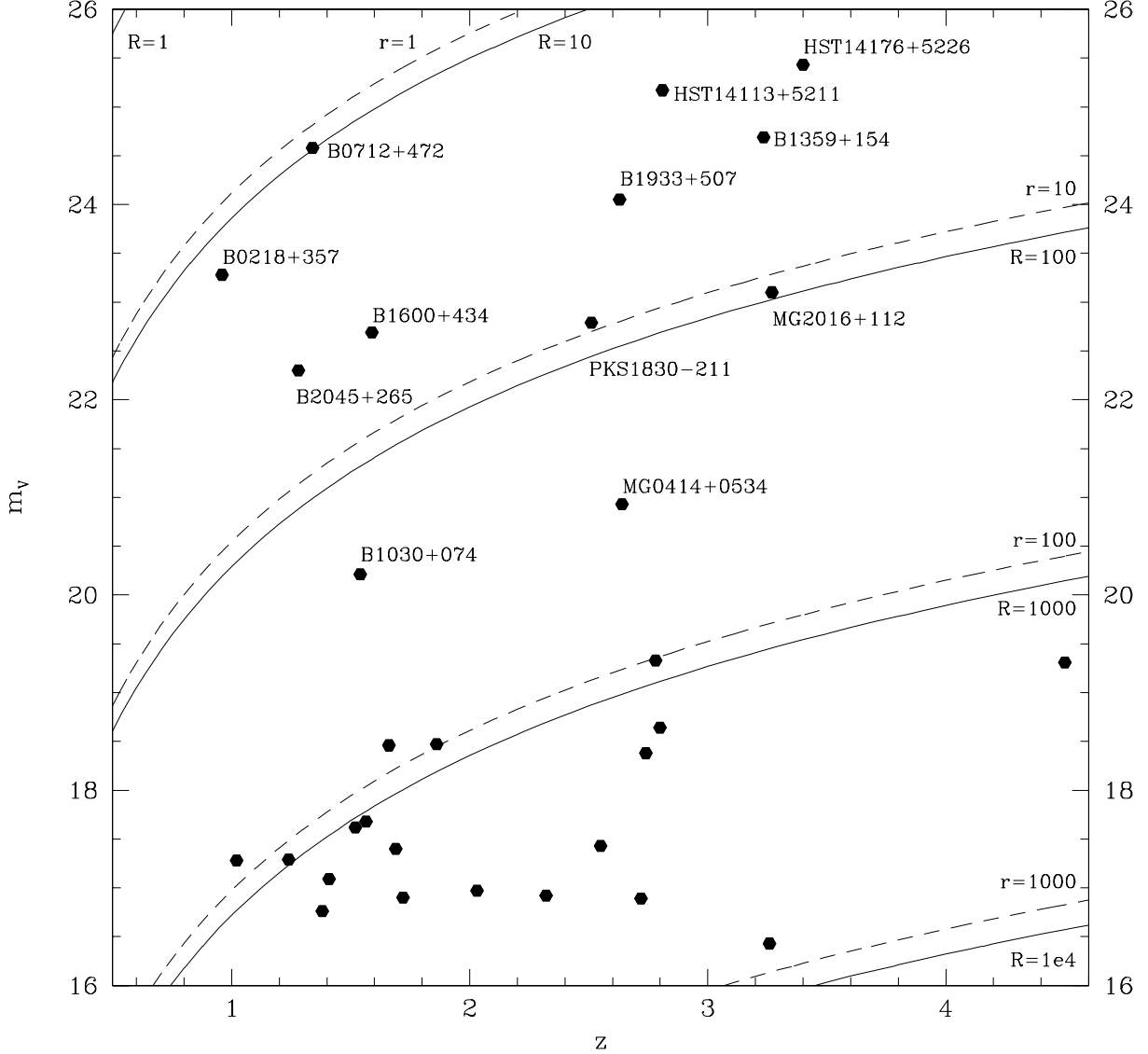


Fig. 1.— Contour plots of the BLR radius (in light-days) as a function of source redshift and apparent magnitude using both reference values for the BLR of NGC 5548 (R when $r_{\text{BLR}}(\text{NGC } 5548) = 21.2$ light-days and r when $r_{\text{BLR}}(\text{NGC } 5548) = 2.5$ light-days) and the Kaspi et al. relationship $r_{\text{BLR}} \propto L^{0.7}$ (for an $\Omega = 0.3$ flat cosmology and $H_0 = 70 \text{ km s}^{-1} \text{ Mpc}^{-1}$). Points represent a sample of 31 QSOs whose redshift–magnitude values have been observed. No extinction or amplification corrections are taken into account.

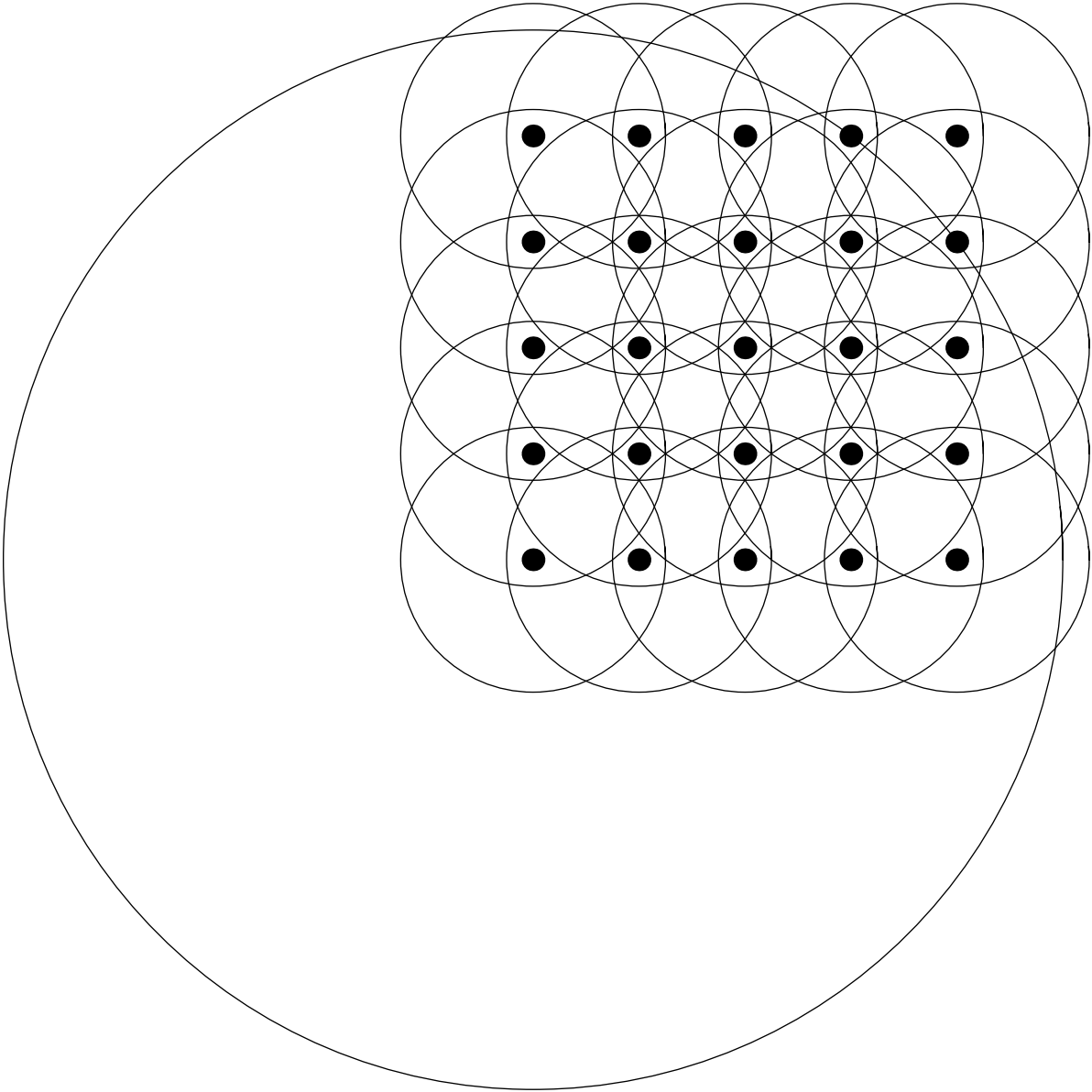


Fig. 2.— Grid of relative displacement between the microlens and the BLR. The big disc represents the BLR. The small discs correspond to the Einstein circle associated with the microlens, represented by a point, in the case $\eta_0 = r_{\text{BLR}}/4$. For each point (corresponding to a displacement of the microlens in the positive quadrant) we compute an emission-line profile.

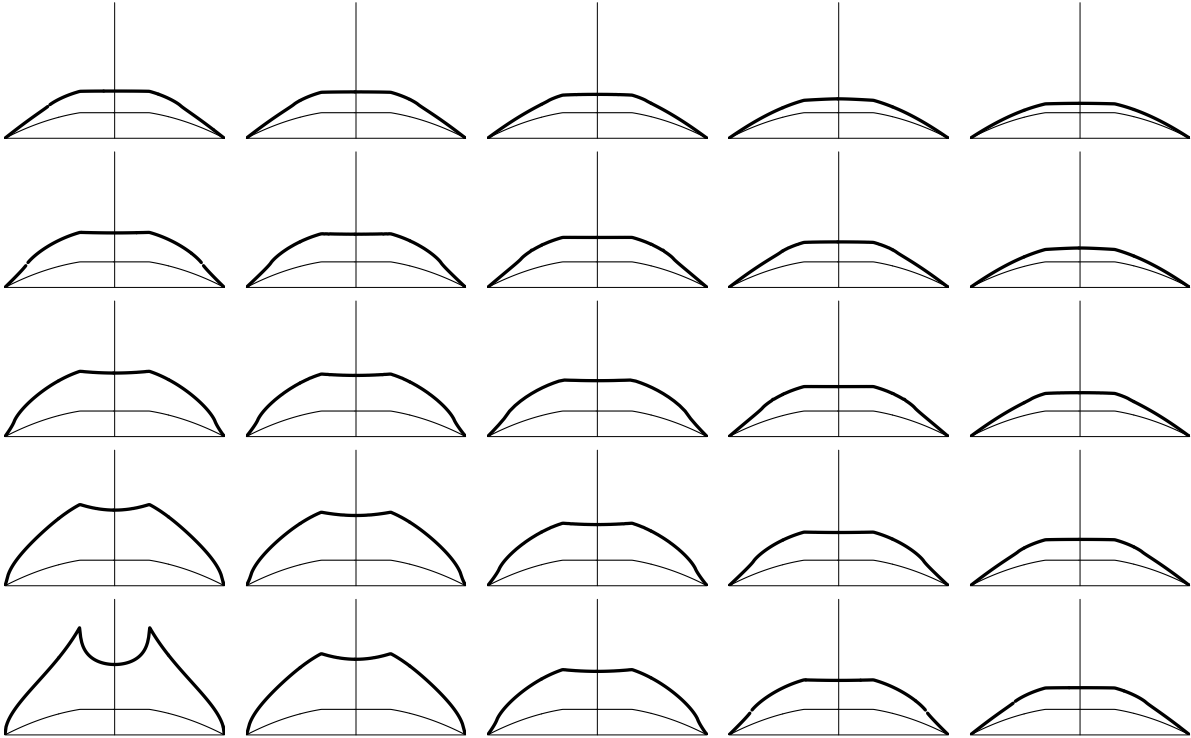


Fig. 3.— Spherical model with $p = 0.5$, $\beta = -1.5$, and $\eta_0 = r_{\text{BLR}}$. On the x -axis we represent $x = c (\lambda - \lambda_0)/(v_{\text{max}}\lambda_0)$, which varies between -1 and 1 . On the y -axis we represent the flux. The heavy solid line is the amplified line profile and the solid line is the unamplified line profile.

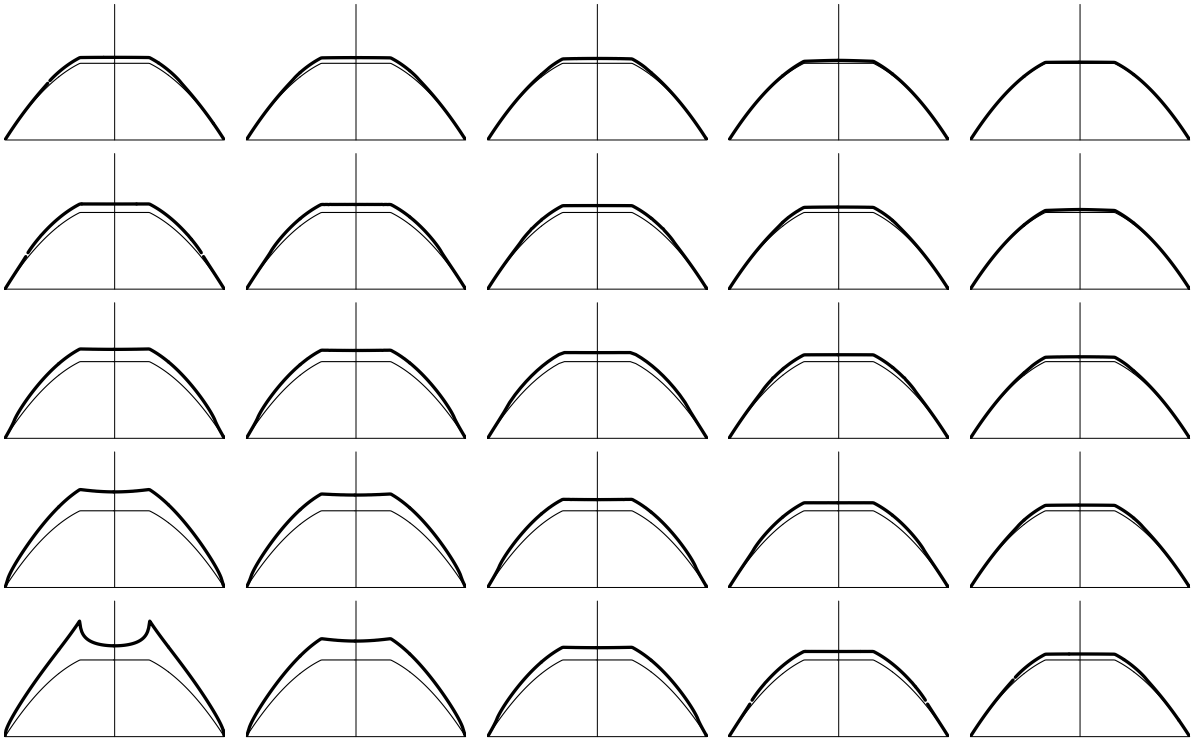


Fig. 4.— The same as in Fig. 3, but for $\eta_0 = r_{\text{BLR}}/4$.

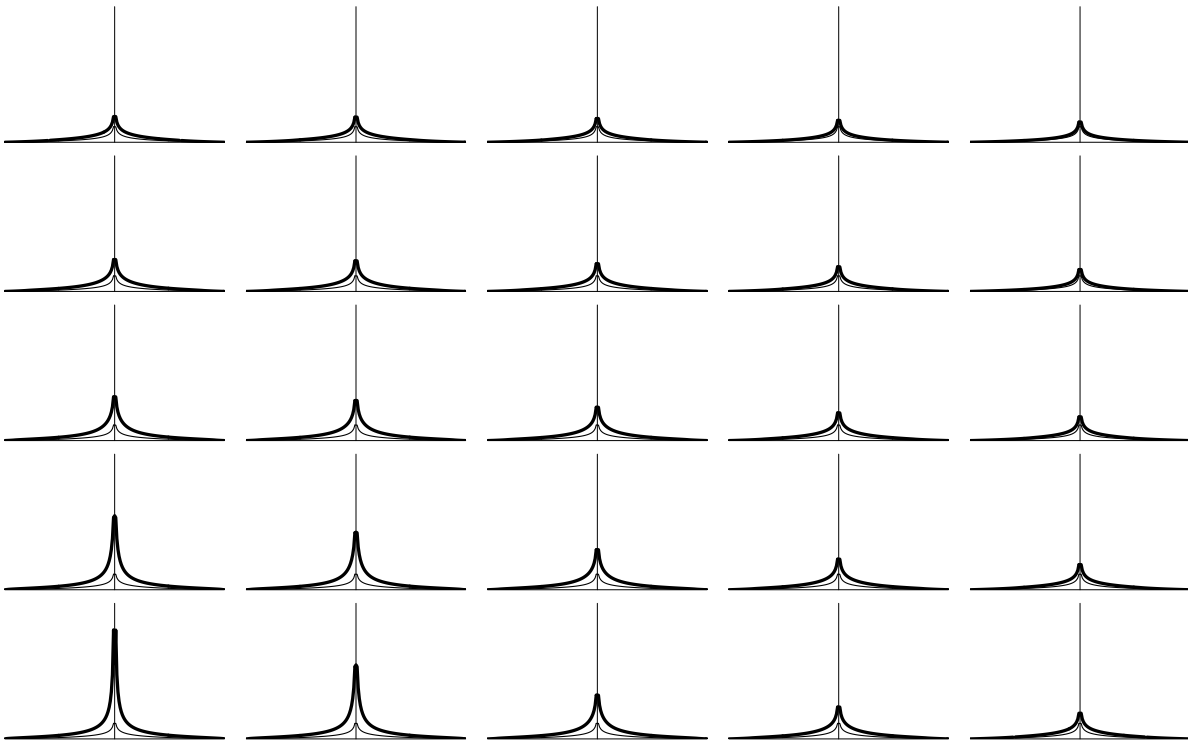


Fig. 5.— Spherical model with $p = 2$, $\beta = -1.5$, and $\eta_0 = r_{\text{BLR}}$. On the x -axis we represent $x = c(\lambda - \lambda_0)/(v_{\max}\lambda_0)$, which varies between -1 and 1 . On the y -axis we represent the flux. The heavy solid line is the amplified line profile and the solid line is the unamplified line profile.

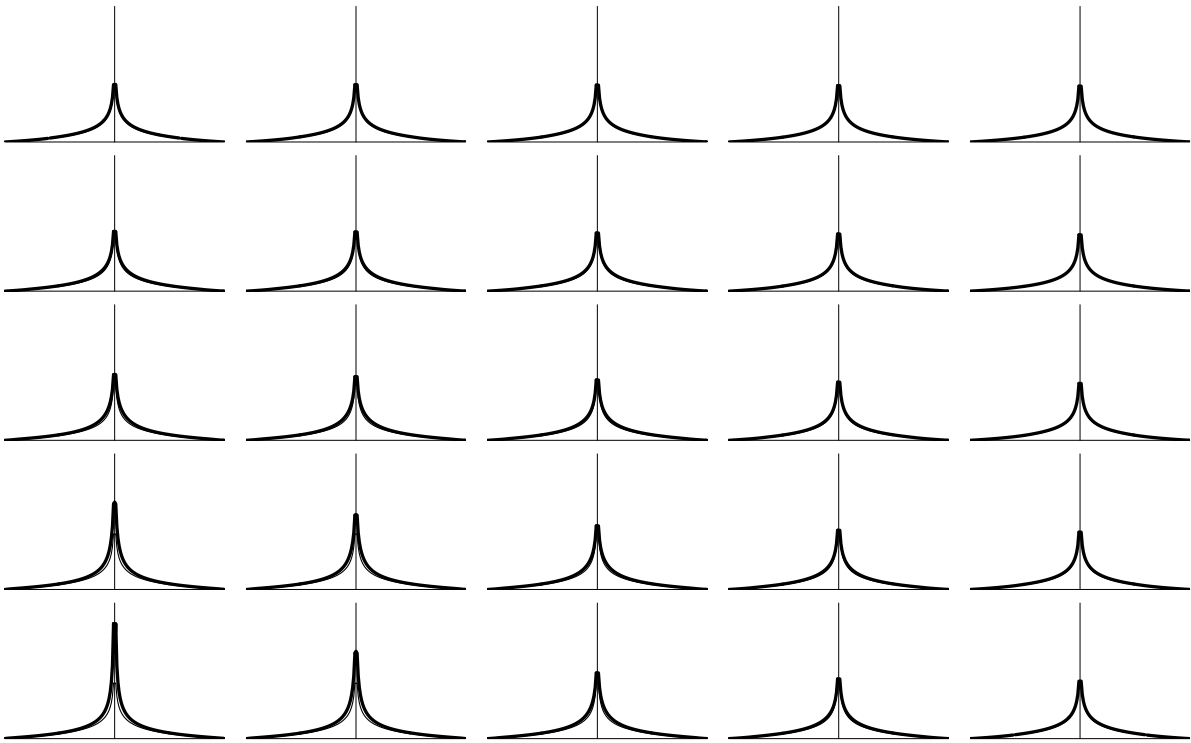


Fig. 6.— The same as in Fig. 5, but for $\eta_0 = r_{\text{BLR}}/4$.

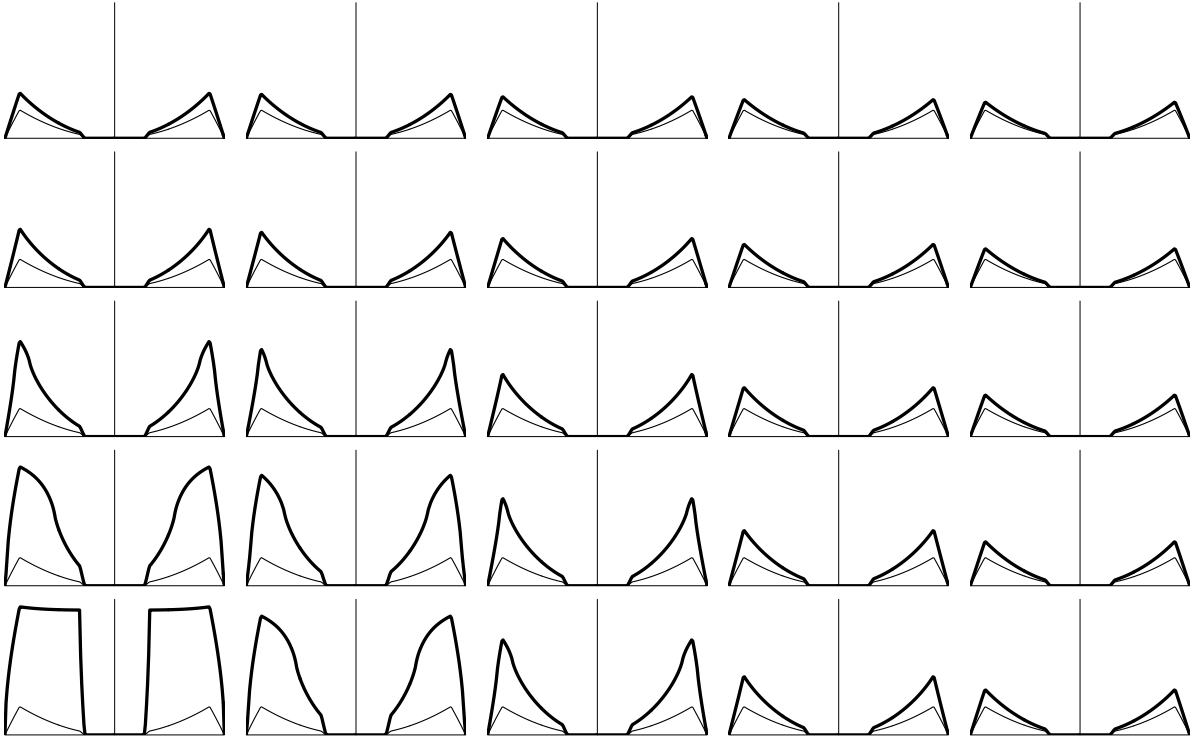


Fig. 7.— Biconical model with $i = 0^\circ$, $p = 0.5$, $\beta = -1.5$, and $\eta_0 = r_{\text{BLR}}$. On the x -axis we represent $x = c(\lambda - \lambda_0)/(v_{\max}\lambda_0)$, which varies between -1 and 1 . On the y -axis we represent the flux. The heavy solid line is the amplified line profile and the solid line is the unamplified line profile.

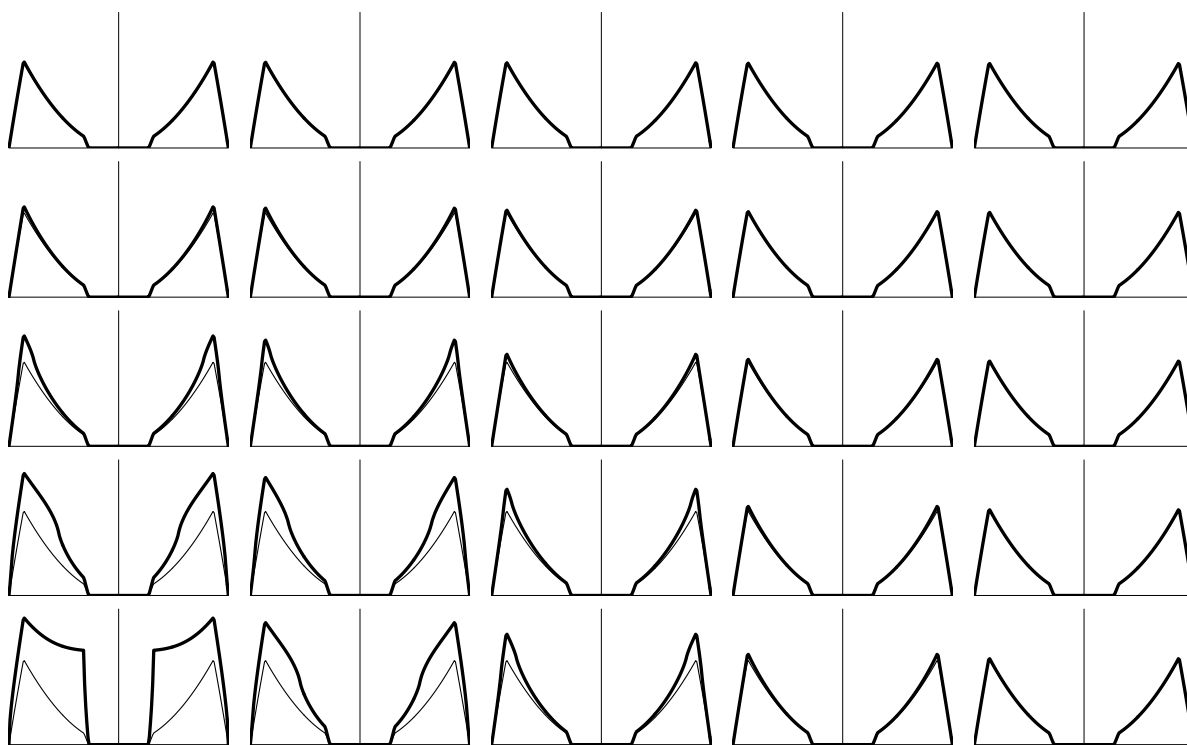


Fig. 8.— The same as in Fig. 7, but for $\eta_0 = r_{\text{BLR}}/4$.

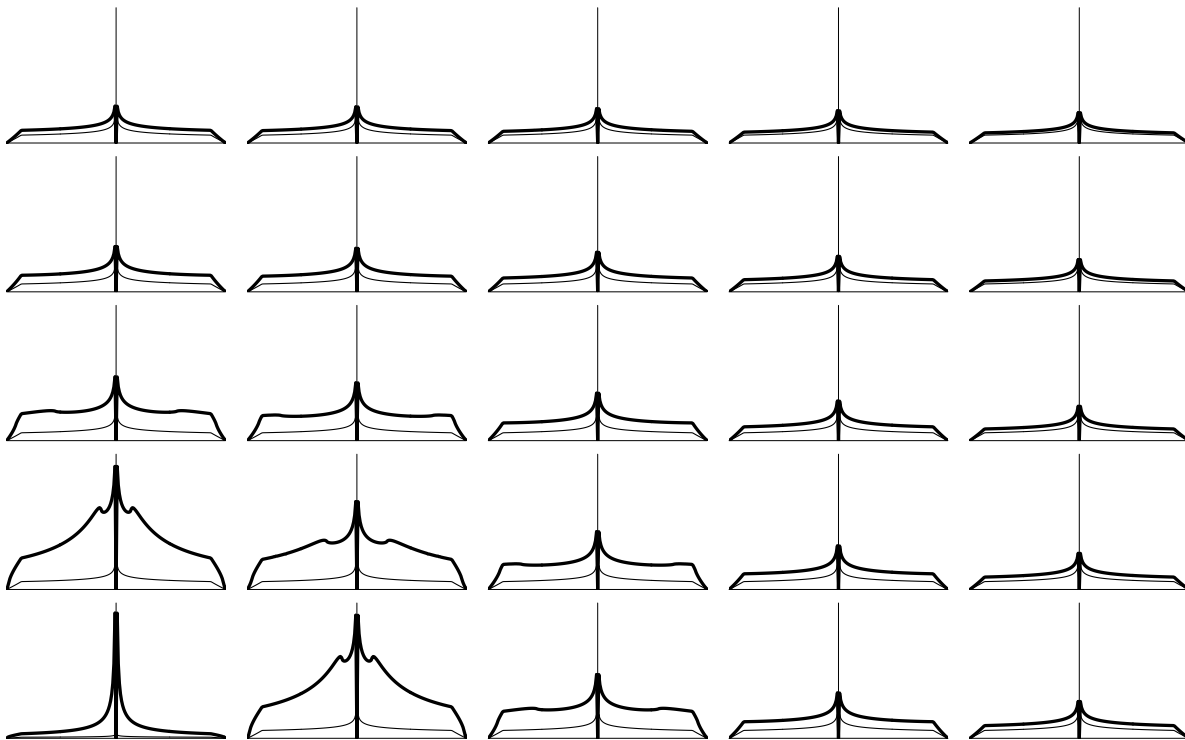


Fig. 9.— Biconical model with $i = 0^\circ$, $p = 2$, $\beta = -1.5$, and $\eta_0 = r_{\text{BLR}}$. On the x -axis we represent $x = c (\lambda - \lambda_0)/(v_{\text{max}}\lambda_0)$, which varies between -1 and 1 . On the y -axis we represent the flux. The heavy solid line is the amplified line profile and the solid line is the unamplified line profile. The figure in the bottom-left corner has been multiplied by a factor 7.2 for display purposes.

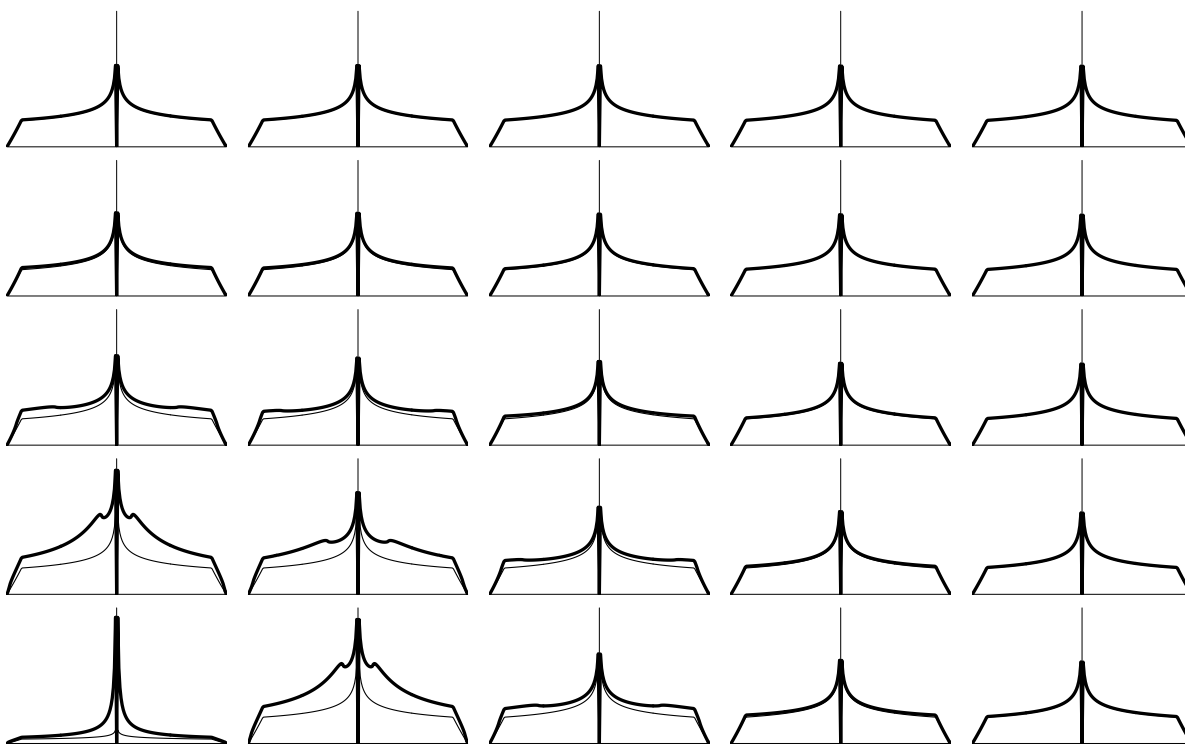


Fig. 10.— The same as in Fig. 9, but for $\eta_0 = r_{\text{BLR}}/4$. The figure in the bottom-left corner has been multiplied by a factor 6.0 for display purposes.

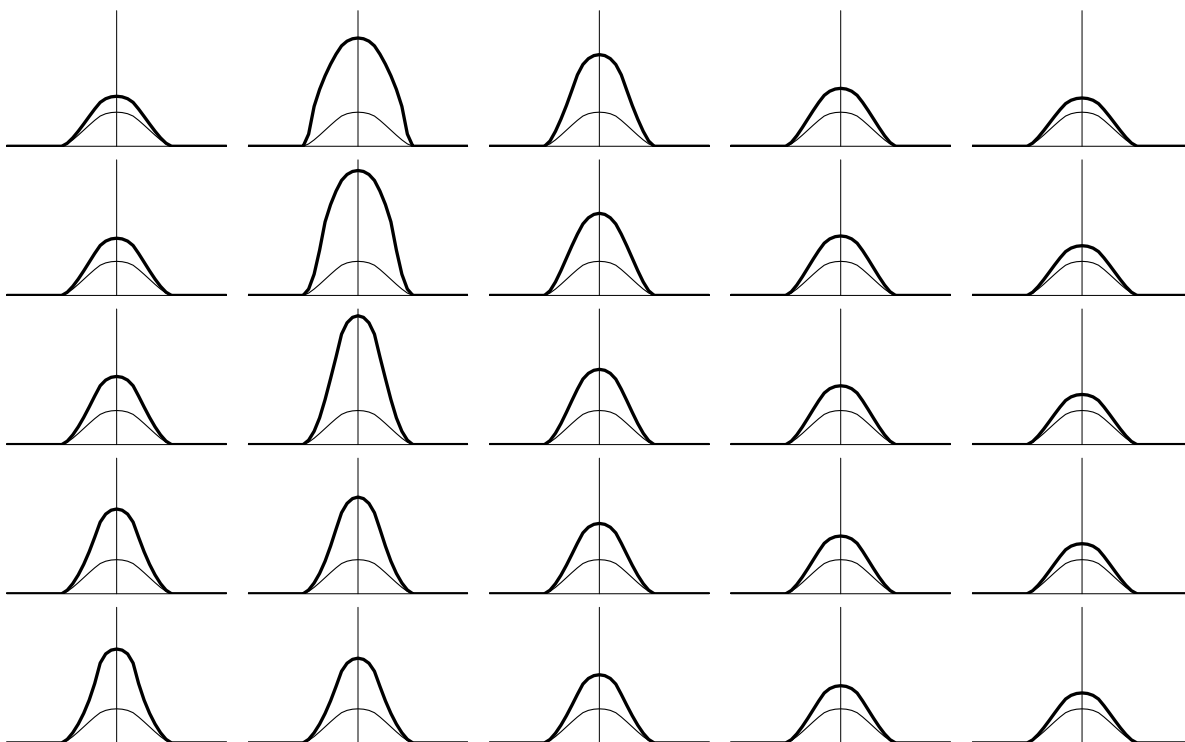


Fig. 11.— Biconical model with $i = 90^\circ$, $p = 0.5$, $\beta = -1.5$, and $\eta_0 = r_{\text{BLR}}$. On the x -axis we represent $x = c (\lambda - \lambda_0) / (v_{\text{max}} \lambda_0)$, which varies between -1 and 1 . On the y -axis we represent the flux. The heavy solid line is the amplified line profile and the solid line is the unamplified line profile.

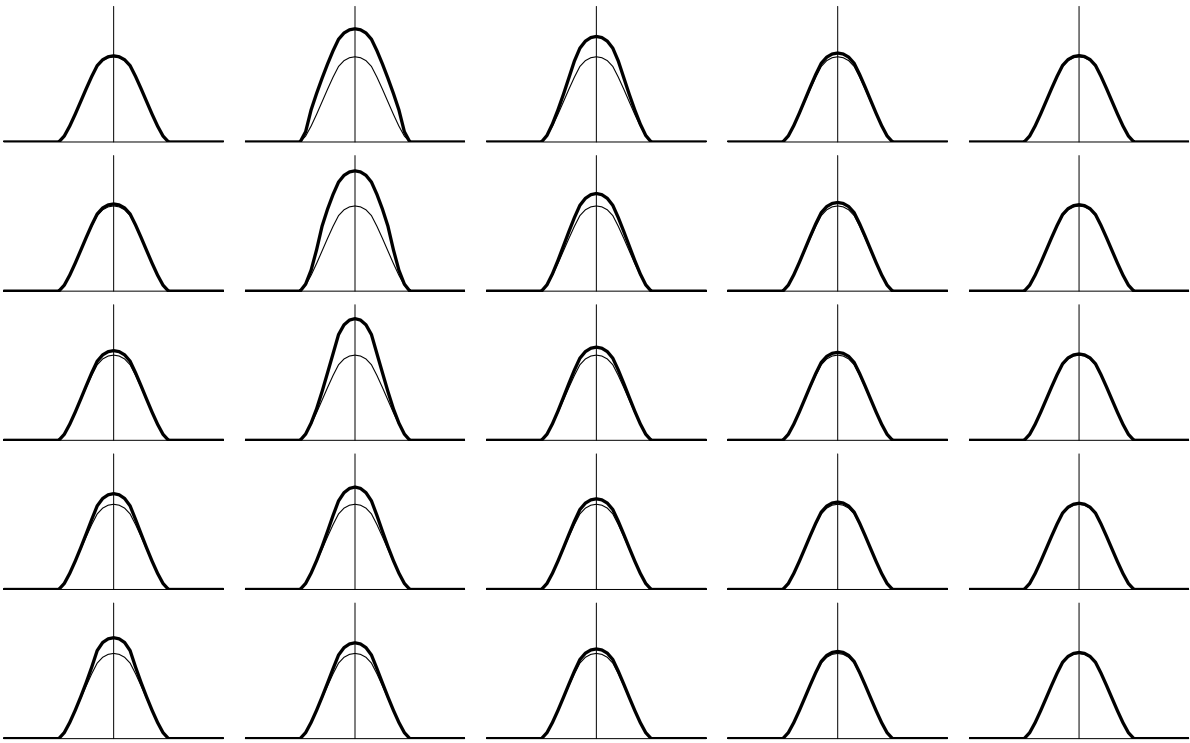


Fig. 12.— The same as in Fig. 11, but for $\eta_0 = r_{\text{BLR}}/4$.

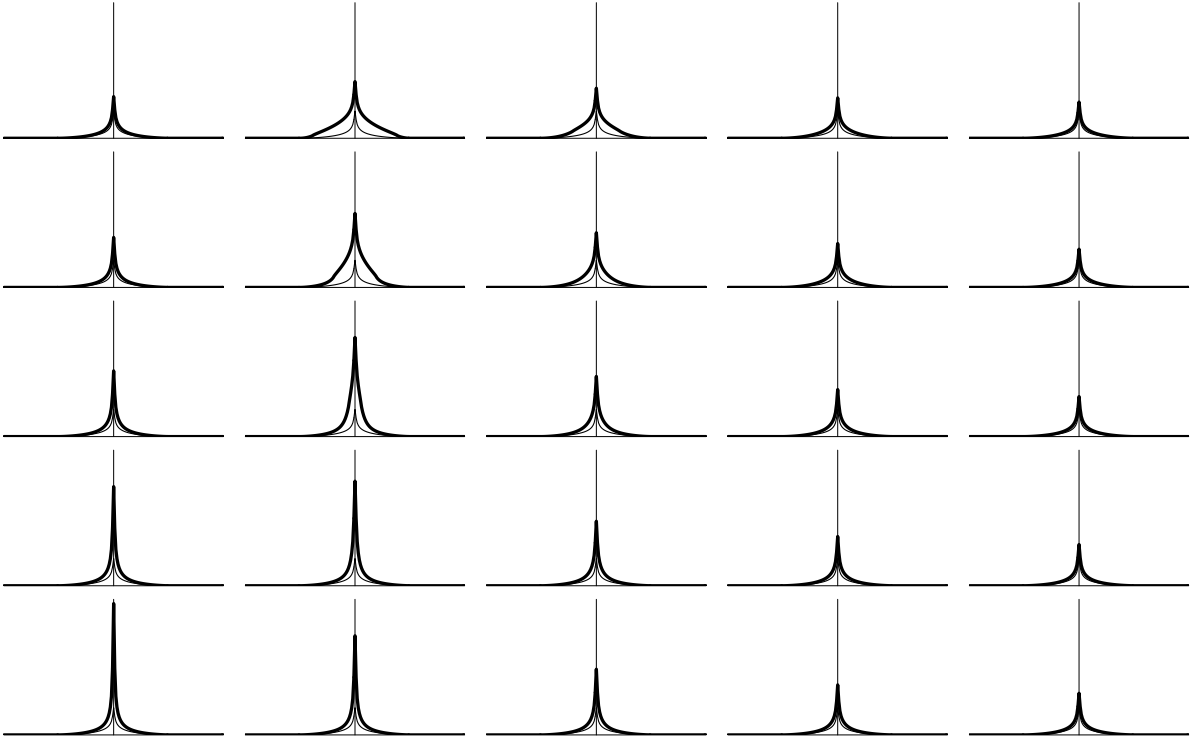


Fig. 13.— Biconical model with $i = 90^\circ$, $p = 2$, $\beta = -1.5$, and $\eta_0 = r_{\text{BLR}}$. On the x -axis we represent $x = c(\lambda - \lambda_0)/(v_{\max}\lambda_0)$, which varies between -1 and 1 . On the y -axis we represent the flux. The heavy solid line is the amplified line profile and the solid line is the unamplified line profile.

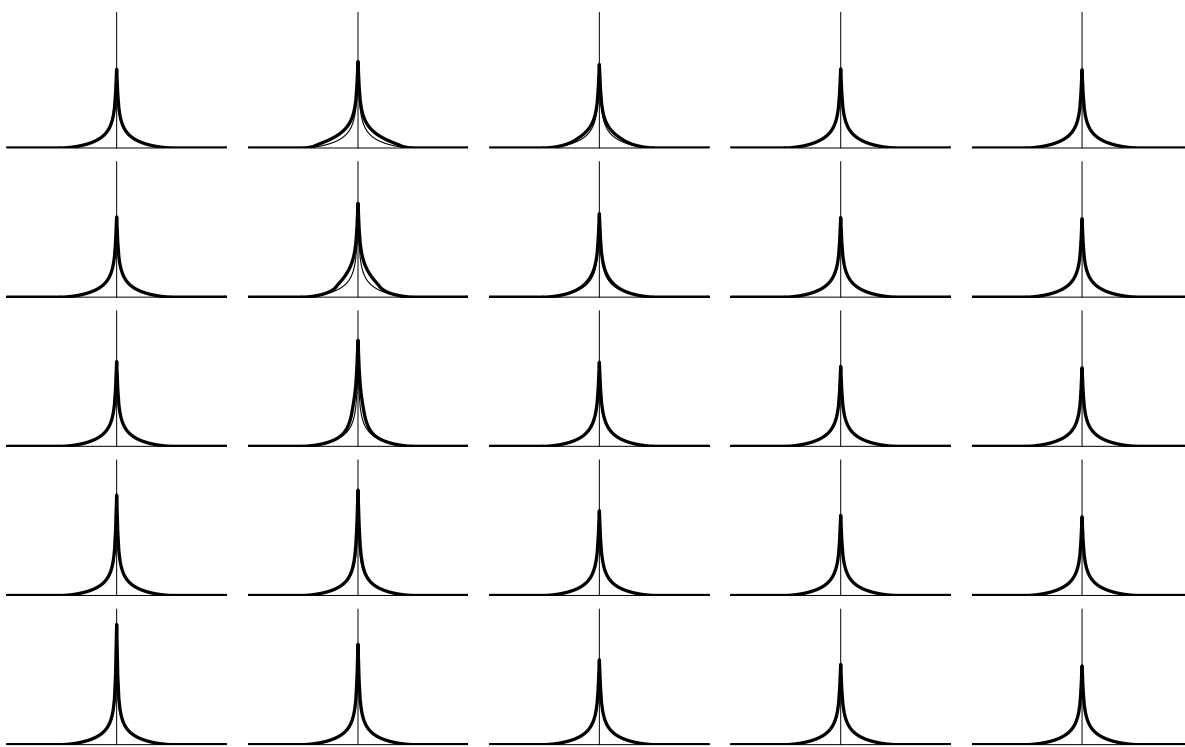


Fig. 14.— The same as in Fig. 13, but for $\eta_0 = r_{\text{BLR}}/4$.

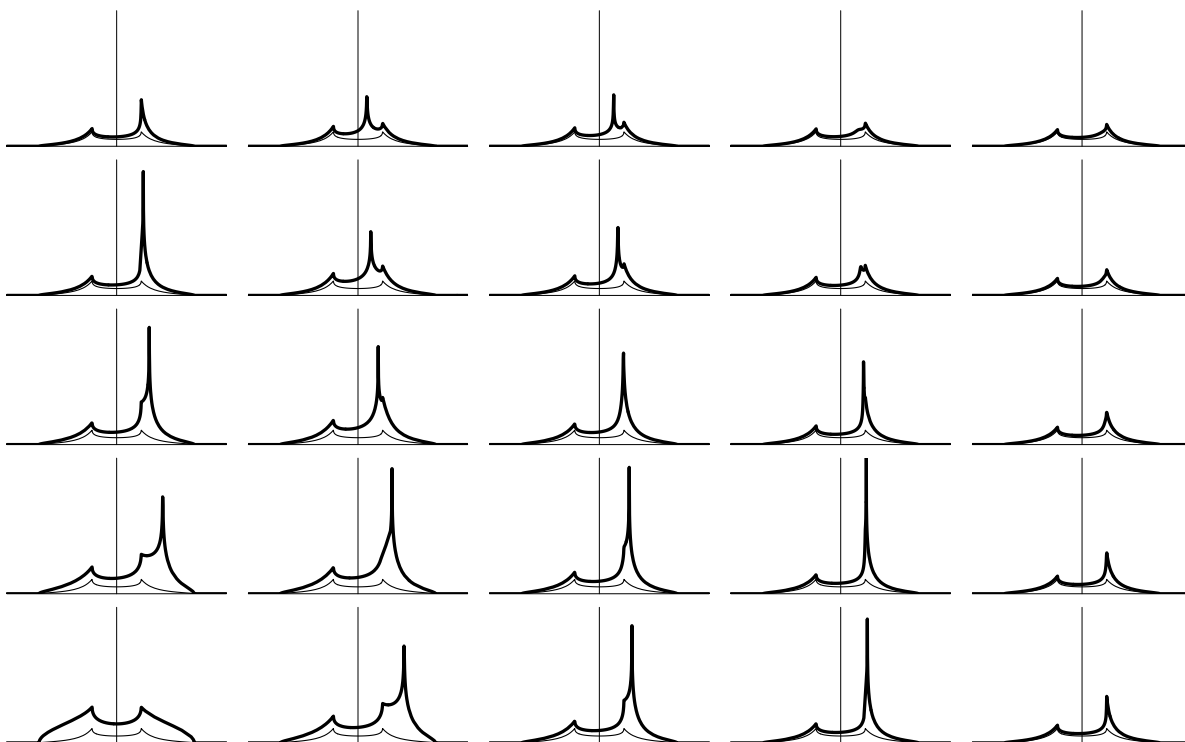


Fig. 15.— Model of Keplerian disk with $i = 45^\circ$, $p = -0.5$, $\beta = -1.5$, and $\eta_0 = r_{\text{BLR}}$. On the x -axis we represent $x = c (\lambda - \lambda_0)/(v_{\text{max}}\lambda_0)$, which varies between -1 and 1 . On the y -axis we represent the flux. The heavy solid line is the amplified line profile and the solid line is the unamplified line profile.

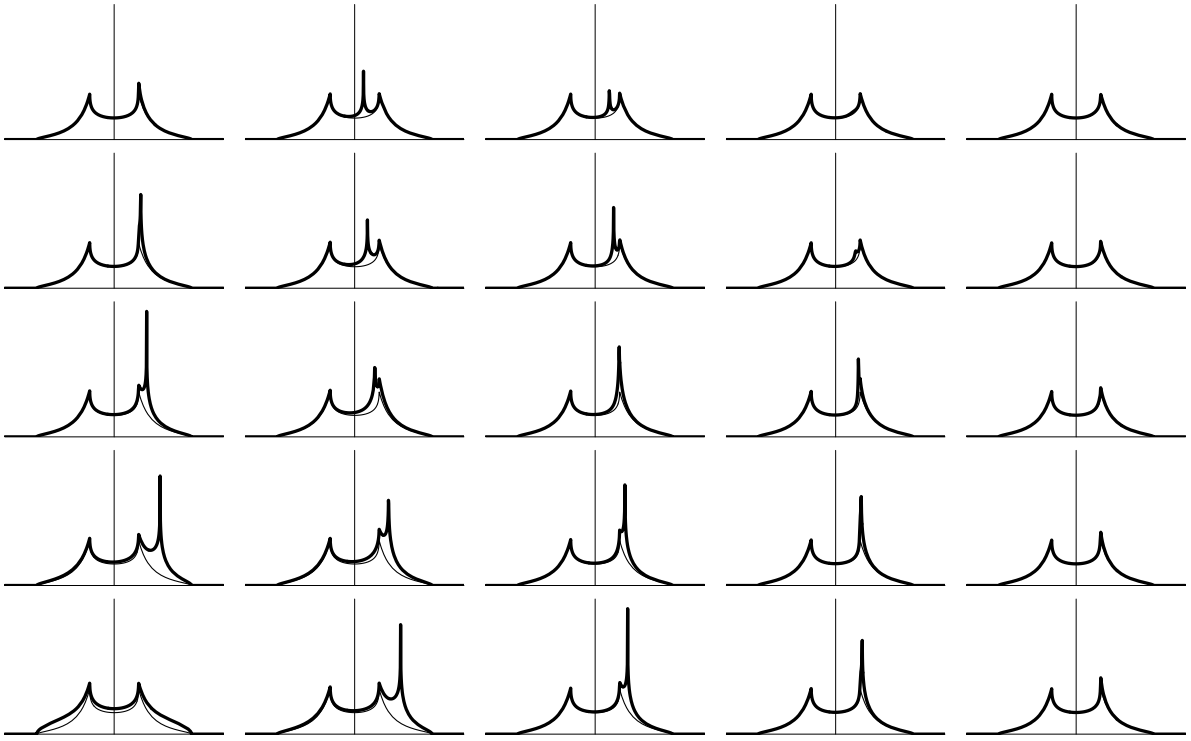


Fig. 16.— The same as in Fig. 15, but for $\eta_0 = r_{\text{BLR}}/4$.

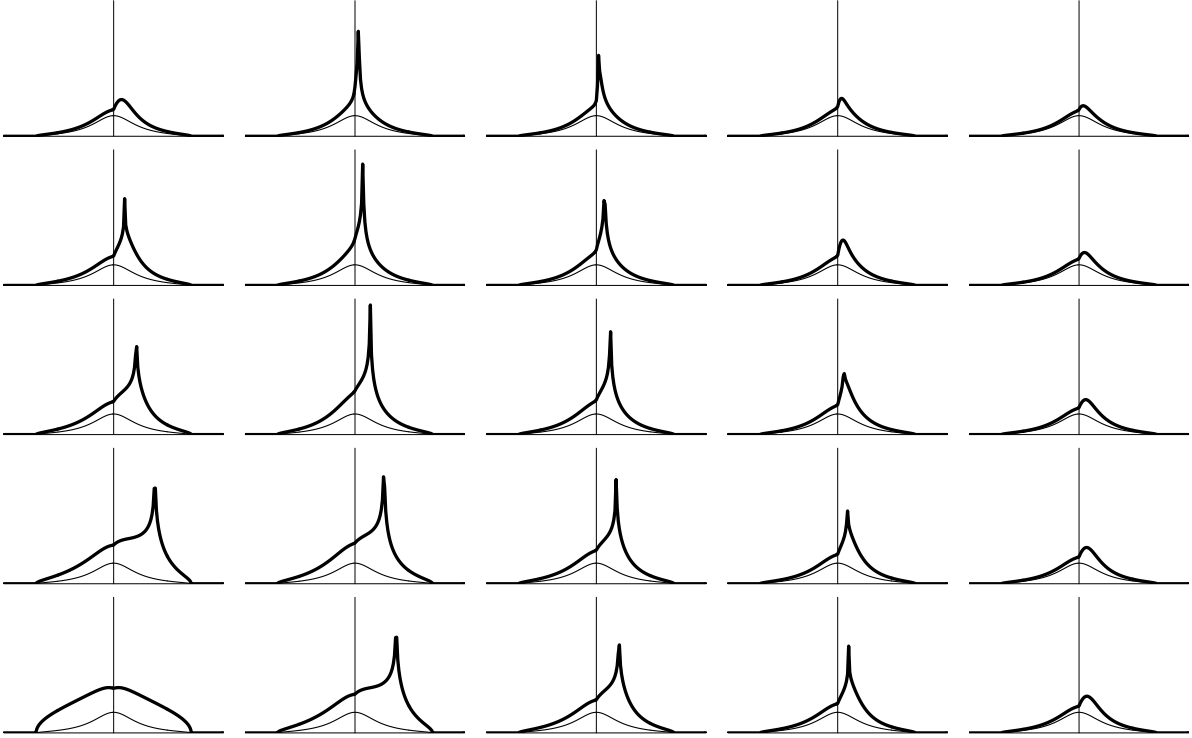


Fig. 17.— Model of modified Keplerian disk with $i = 45^\circ$, $p = -0.5$, $\beta = -1.5$, and $\eta_0 = r_{\text{BLR}}$. On the x -axis we represent $x = c (\lambda - \lambda_0)/(v_{\text{max}}\lambda_0)$, which varies between -1 and 1 . On the y -axis we represent the flux. The heavy solid line is the amplified line profile and the solid line is the unamplified line profile.

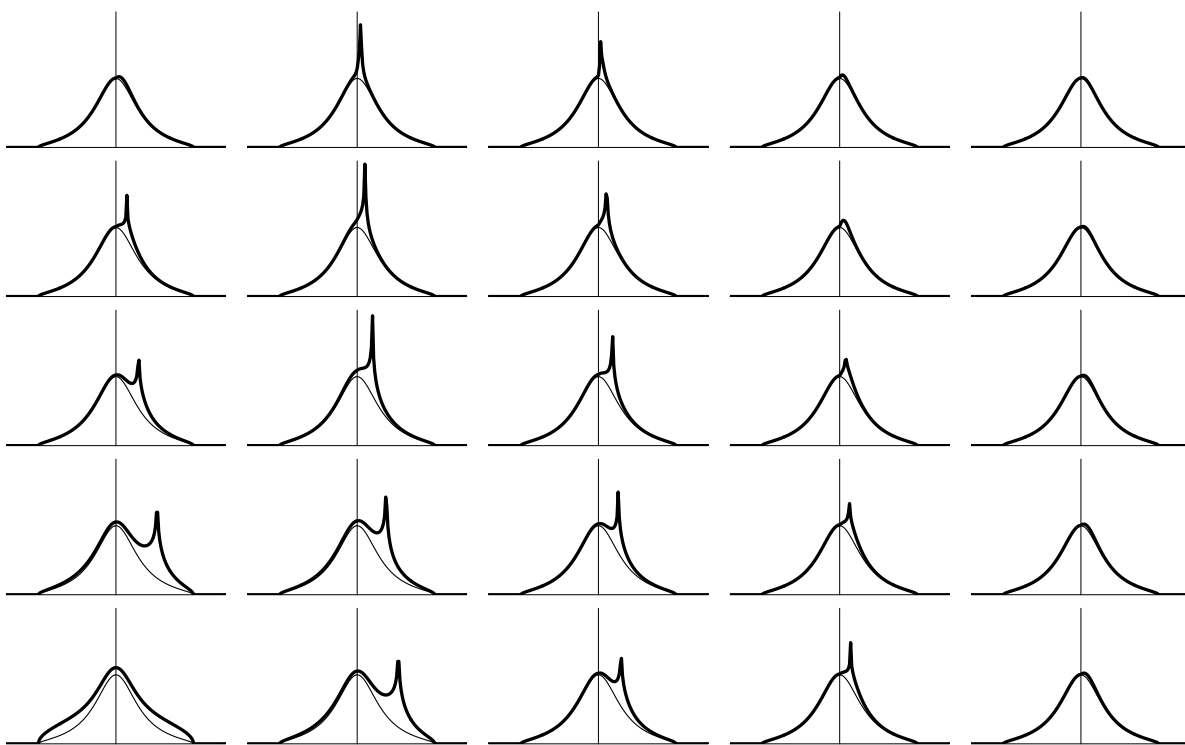


Fig. 18.— The same as in Fig. 17, but for $\eta_0 = r_{\text{BLR}}/4$.

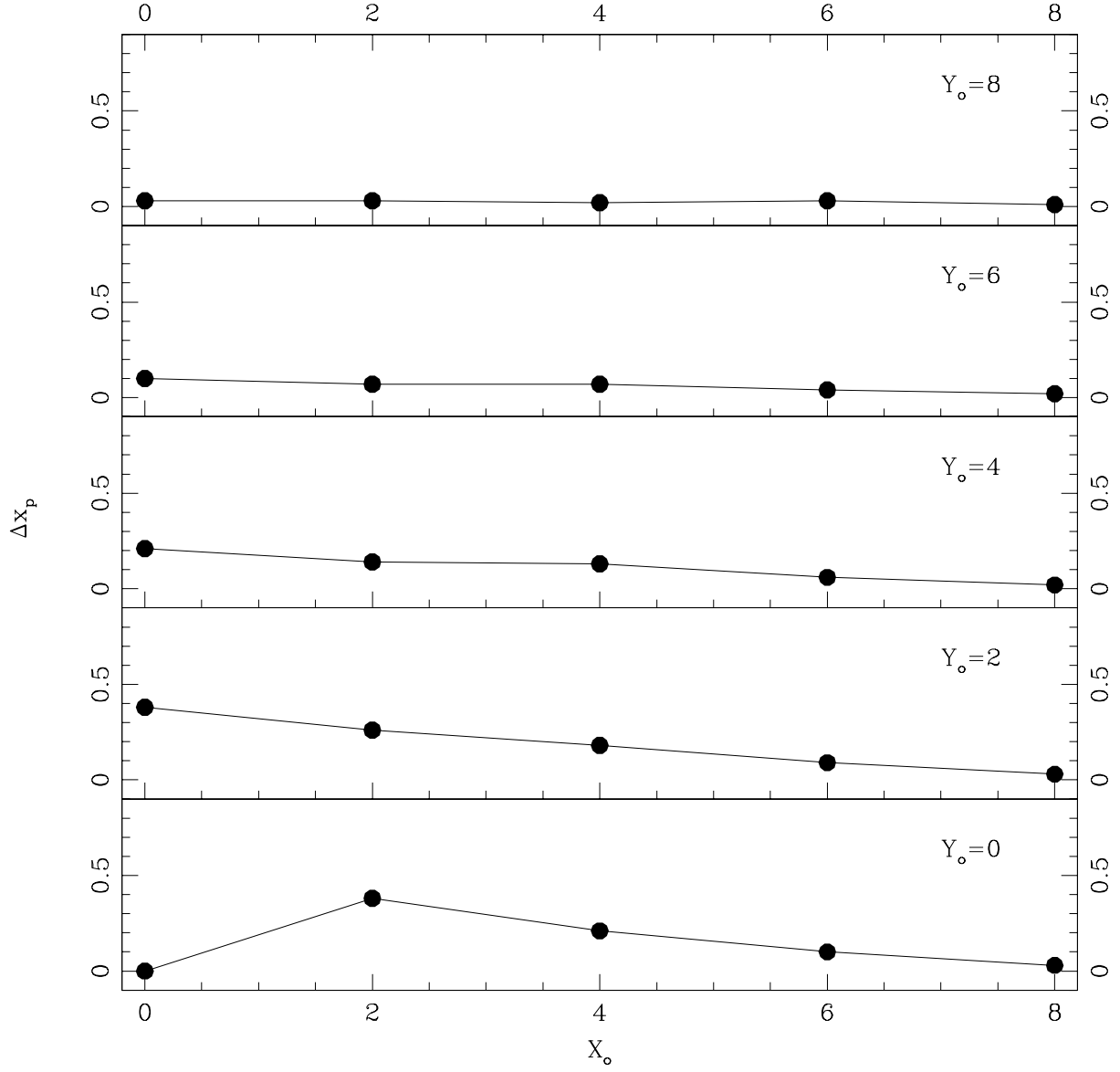


Fig. 19.— Displacements of the line peaks, Δx_p , in the modified Keplerian disc model with $i = 45^\circ$, $p = -0.5$, $\beta = -1.5$, and $\eta_0 = r_{\text{BLR}}/4$ in the different positions (X_0, Y_0) .

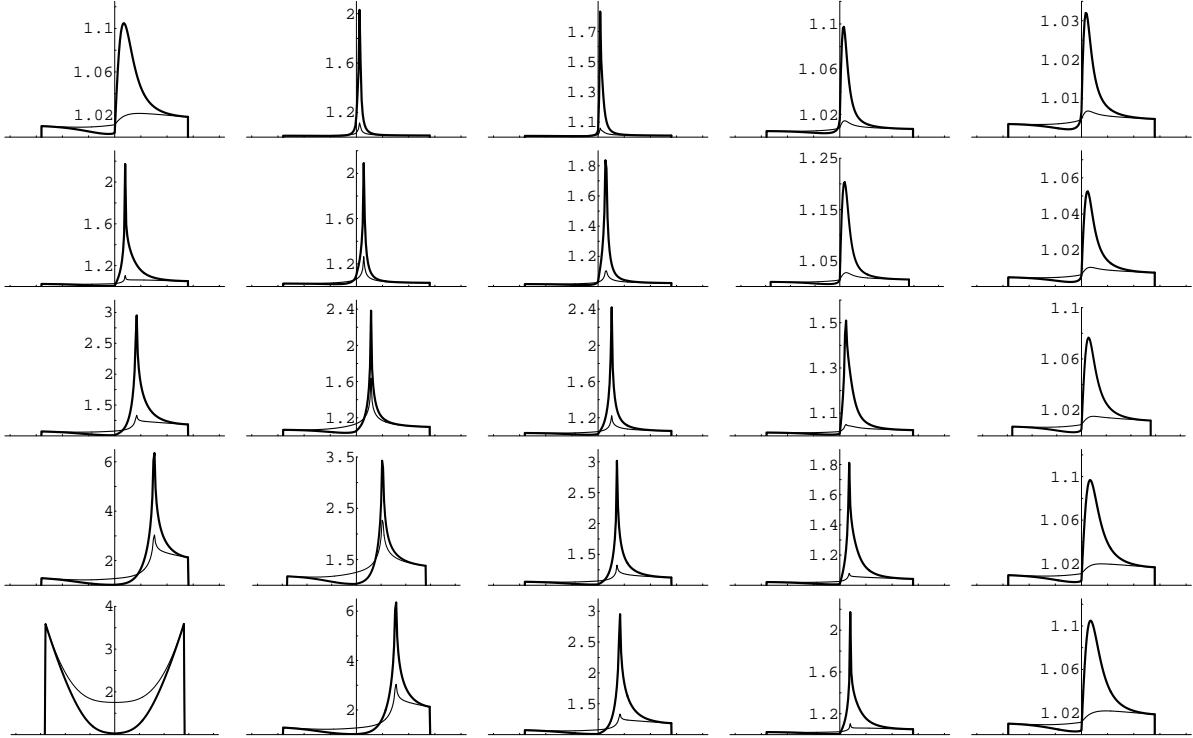


Fig. 20.— Model of modified Keplerian disk with $i = 45^\circ$, $p = -0.5$, and $\eta_0 = r_{\text{BLR}}/4$. On the x -axis we represent $x = c (\lambda - \lambda_0)/(v_{\text{max}}\lambda_0)$, which varies between -1 and 1 . On the y -axis we represent the ratio between the amplified flux and the unamplified flux of the line profile. The heavy solid line is for $\beta = 0$ and the solid line is for $\beta = -4$.